



Sol–gel synthesis, structure, sintering and properties of bioactive and inert nano-apatite–zirconia glass–ceramics

Maziar Montazerian^{a,*}, José Fabián Schneider^b, Bijan Eftekhari Yekta^a,
Vahak Kaspari Marghussian^a, Alisson Mendes Rodrigues^c, Edgar Dutra Zanotto^c

^a*School of Metallurgy and Materials Engineering, Iran University of Science and Technology, Tehran 1684613114, Iran*

^b*Instituto de Física de São Carlos, Universidade de São Paulo, São Carlos, SP, 13.566-590, Brazil*

^c*Department of Materials Engineering, Center for Research, Technology and Education in Vitreous Materials (CeRTEV), Federal University of São Carlos, São Carlos, SP, 13.565-905, Brazil*

Received 23 March 2015; accepted 10 May 2015

Abstract

We synthesized four glasses of the system $61.2\text{SiO}_2-(24.3-x)\text{CaO}-4.5\text{P}_2\text{O}_5-10\text{ZrO}_2-x\text{K}_2\text{O}$ ($x=0, 2, 4, 6$ mol% = Ca replaced by K) using a sol–gel route and compared their properties with a $68\text{SiO}_2-27\text{CaO}-5\text{P}_2\text{O}_5$ (mol%) Zr-free base glass. Their structure, sintering and crystallization behavior were investigated with the aim of converting the gel-glasses into dense glass–ceramics. Then, the *in vitro* bioactivity and mechanical properties of the optimized sintered samples were characterized. The structure of the gel-glasses was investigated by Fourier transform infrared spectroscopy (FTIR), nuclear magnetic resonance spectroscopy (NMR) and high-resolution transmission electron microscopy (HR-TEM). The sintering and crystallization kinetics of the glasses were studied by hot stage microscopy (HSM), differential scanning calorimetry (DSC) and X-ray diffraction (XRD). The microstructures of the resulting glass–ceramics were investigated by scanning electron microscopy (SEM) and transmission electron microscopy (TEM) coupled with energy dispersive spectroscopy (EDS). The apatite-forming ability of the sintered glass–ceramics in simulated body fluid (SBF) was investigated using FTIR spectroscopy and SEM. The three-point bending strength, Vickers microhardness and fracture toughness were also measured. Structural analysis by NMR and FTIR revealed that Zr acts as a glass former and K is a modifier, as expected. The K_2O addition strongly improved the material's sinterability, *e.g.*, 2 mol% K_2O decreased the optimum sintering temperature from 1300 °C to 1050 °C. Uniformly dispersed ZrO_2 nano-crystals, with particle sizes of 25–55 nm, were precipitated in the glass–ceramics. *In vitro* bioactivity tests confirmed that the K_2O -free glass–ceramics (partially sintered at 1000 °C) were bioactive and hydroxycarbonate apatite (HCA) grew on their surface after 24 h in SBF. However, the > 90% dense glass–ceramics with various contents of K_2O exhibited low solubility and a much smaller tendency toward HCA formation. Improvement of some mechanical properties was observed for the sample containing 2 mol% K_2O , in which apatite and zirconia crystallized. The 3p-bending strength and fracture toughness of the 94% dense sample were approximately 140 MPa and $2\text{ MPa m}^{1/2}$, respectively. We propose that crack deflection by the ZrO_2 crystals and the presence of Zr ions in the residual glass network are prevalent for improving the materials' mechanical properties. Some potential applications, such as bioactive scaffolds, are suggested for these glass–ceramics.

© 2015 Elsevier Ltd and Techna Group S.r.l. All rights reserved.

Keywords: A. Sintering; D. Glass–ceramic; D. Apatite; Sol–gel; Bioactive; Crystallization; Zirconia

1. Introduction

Glasses and glass–ceramics are promising materials for various applications, such as commodity products or parts of

sophisticated electrical, biomedical and optical devices [1,2]. Most monolithic glasses are produced via the classical melting–quenching process, and some can be converted into glass–ceramics by controlled heat-treatments. Such treatments are usually performed at relatively low temperatures, not far from the glass transition, T_g , to induce internal nucleation, followed by a second stage at a somewhat higher temperature to promote crystallization of different phases [3–5].

*Corresponding author. Tel.: +98 912 6760071; fax: +98 21 4465610.

E-mail address: montazerian@iust.ac.ir (M. Montazerian).

Another, less frequent, process based on powder processing is sometimes used, in which glass powders are shaped and then sintered and simultaneously crystallized. The processing parameters are selected in such a way that the glass softens prior to crystallization and undergoes viscous flow and densification before the crystallization process is completed. Sintering and crystallization usually proceed concurrently, and the free surfaces of the glass frits encourage crystallization; hence, precise control of the chemical composition, frit particle size, temperature and time are essential [3–5].

Over the past thirty years, the synthesis of different glasses via the sol–gel route has attracted the attention of many researchers [6–8]. This method allows for low-temperature chemistry-based synthesis, where a sol containing chemical precursors gellifies under certain pH and concentration conditions near room temperature. Gels are wet inorganic networks of silica, which can then be dried and heated, e.g., at 600–700 °C, and are converted into a glass. In principle, sol–gel-derived glass powders exhibit higher purity and greater chemical homogeneity than melt-derived powders [6–9].

Among the numerous glass types prepared by the sol–gel method, many studies on bioactive glasses with the base composition $\text{SiO}_2\text{--CaO--P}_2\text{O}_5$ have been performed, mainly because nano-porous glasses with high surface area containing hydroxyl groups can be easily synthesized by this procedure [9–15]. Nano-porous glasses are usually highly bioactive even if they have relatively high silica content, more than 60 mol% [8–10]. Therefore, extensive efforts have been made towards the synthesis of powders, porous particulates and mesoporous glasses for scaffold development, bone regeneration, drug delivery, and treatment of hypersensitive teeth, etc. [9–15].

One important drawback of the sol–gel synthesis over the melt process is that it is very difficult to obtain crack-free glass monoliths with diameters in excess of ~ 1 cm [6,7]. One solution is to partially sinter gel-glass powders to a desirable density for particular applications, such as scaffolds, coatings and bone grafts. In this process, crystallization may be encouraged in some cases, depending on the intended application and whether the considered crystals are bioactive [8,12–14]. However, very few research results addressing the sintering process of bioactive gel-glasses have been reported. This apparent lack of reports may be due to the fact that gel-derived glass powders are highly porous and exhibit a great tendency toward incipient crystallization, which normally deteriorates their sinterability. This problem was predicted by one of us in 1992 [16]: “*Due to the intrinsic nature of gels (high OH-content, residual carbon, high fictive state), sol–gel glasses crystallize faster than melt-derived glasses at any temperature. Additionally, gels must be (in general) slowly heated from room temperature to approximately half the liquidus temperature to densify to a glass. That is a riskier path than quenching from the liquid state because the nucleation region is crossed on heating, allowing crystal growth from a plethora of nuclei* [16]”.

Our group has developed a bioactive 68SiO₂–27CaO–5P₂O₅ (mol%) gel-glass powder. We previously reported that this powder exhibits poor sinterability and maximum densification

is only reached at temperatures above 1300 °C. The resulting crystalline phases—cristoballite and pseudo-wollastonite—are neither bioactive nor suitable for good mechanical properties [17]. One solution for overcoming this problem would be to modify the composition by including “fluxing” agents such as Na₂O, B₂O₃, K₂O or CaF₂ in the gel-glass composition [18–22]. In this regard, sintering with concurrent crystallization can be employed to convert the gel-glass powders into dense glass–ceramics.

Potassium oxide (K₂O) belongs to the alkaline oxides group, which, in general, acts as a glass network modifier. This oxide reduces the viscosity and, for some compositions, helps to improve the sinterability of glass powder compacts [3]. Despite extensive studies performed on the biological performance of a companion oxide, Na₂O-containing gel-glass, only a few published studies are available on the effect of K₂O on the properties of gel-derived bioactive glasses [21–23]. It has been reported that replacement of Na₂O by K₂O increases the crystallization temperature in a SiO₂–CaO–P₂O₅–Na₂O glass [23], and its substitution for CaO improves sinterability [21].

In addition, for many years, researchers have been trying to incorporate ZrO₂ into numerous glass and glass–ceramic compositions to benefit from its (potential) toughening aptitude. Their aims were to develop bone graft substitutes, bone cements and bioactive materials with improved mechanical properties and durability [24–31]. For example, inert and durable glass–ceramics containing ZrO₂ are applicable for dental restoration build-up on a zirconia core (IPS Cosmo® is a commercial example) [2,24]. Reinforced bioactive glass–ceramics by ZrO₂ particles have been studied for more than 20 years [25–31]. These materials are usually made by sintering or melting processes, which have some limitations. For instance, in the course of melting, zirconia often results in an increased melting temperature and viscosity of the liquid [24–27]. Through the sintering route, the zirconia powder can be mixed with a glass frit, and the pressed mixture must then be densified and crystallized. However, in this case, zirconia particles tend to agglomerate during mixing and also increase the sintering temperature [28–31]. Therefore, it is clear that fabrication of glasses and glass–ceramics with a high content of ZrO₂ is difficult when conventional sintering or melting is employed.

The sol–gel process has been used as an alternative route to incorporate high contents of ZrO₂ in glasses, and it appears that zirconium addition can be performed at room temperature, thus avoiding high melting and sintering temperatures [32–37]. We have recently reported on the cell proliferation and *in vitro* bioactivity of a new gel-glass powder in the SiO₂–CaO–P₂O₅–ZrO₂ system [37]. We demonstrated that a simple sol–gel route can be used to synthesize a bioactive SiO₂–CaO–P₂O₅ glass powder containing 10 mol% ZrO₂. In that article, we focused on the biological performance of the ZrO₂-containing bioactive glass and its glass–ceramic derivative powders (apatite–wollastonite–zirconia glass–ceramic). The addition of ZrO₂ into the base glass composition reduced the rate of HCA formation from one day to three days. However, surprisingly, hydroxyapatite formed more rapidly on the crystalline powder surface than on the glass particles. We have demonstrated that ZrO₂ can be employed

to control the rate of apatite formation by means of its addition to the glass. We suggested that these new powders are potential candidates for bone graft substitutes, bone cements and bone regeneration with the special feature of radiopacity [37].

Herein, we were hopeful that K₂O addition could lead to a dense glass–ceramic at relatively low temperatures and uniform crystallization of ZrO₂ particles could improve the mechanical properties without losing bioactivity. Therefore, we investigated the molecular structure, sintering, crystallization, *in vitro* bioactivity and mechanical properties of the above mentioned gel-glass powder and sintered glass–ceramics containing 10 mol% ZrO₂ and 2–6 mol% K₂O compared with ZrO₂- and K₂O-free glasses.

2. Experimental procedures

2.1. Gel preparation

The gels were prepared by hydrolysis and polycondensation of stoichiometric amounts of tetraethoxysilane (TEOS, Si(OC₂H₅)₄), triethylphosphate (TEP, OP(OC₂H₅)₃), calcium nitrate tetrahydrate (Ca(NO₃)₂·4H₂O), potassium nitrate (KNO₃) and zirconium oxynitrate (ZrO(NO₃)₂·xH₂O; x=3). The chemical compositions of the base glass (G), sample containing 10 mol% ZrO₂ (G–Zr) and glasses containing 2–6 mol% K₂O (G–Zr–KX, X=2, 4 and 6) are listed in Table 1. The hydrolysis of TEOS and TEP was catalyzed with a solution of 0.1 mol L⁻¹ HNO₃ using the molar ratio (HNO₃+H₂O)/(TEOS+TEP)=15. Beginning with the hydrolysis of TEOS, the other reagents, *viz.* TEP, calcium, potassium and zirconium nitrates, were sequentially added at 45 min intervals, maintaining the reaction mixture under constant stirring. Then, the sols were poured into Teflon[®] tubes and stored up for 10 days. At the end of this period, the gels were aged for three days at 70 °C and then dried in one day at 150 °C. After completion of the drying step, the gels were manually ground in an agate mortar to less than 75 μm.

2.2. Conversion of the gels into glasses

Just after milling, individual portions containing approximately 20 g of dried gels with particle size less than 75 μm were placed in an alumina crucible for heat treatment. The materials were treated in an electric furnace at 700 °C under an oxidizing atmosphere (air). The heating programs were adapted according to the results of previous differential

thermal (DTA) and thermogravimetric (TG) analyses of the starting gels. These analyses were performed in a Netzsch STA 409 PC instrument under a nitrogen atmosphere (synthetic N₂) with a gas flow rate of 50 mL min⁻¹. Typical runs involved ~6 mg of a gel sample at a rate of 10 °C min⁻¹ from room temperature to 1000 °C to determine the initial heat treatment temperature and the onset of formation of the crystalline phases. The established thermal treatment programs consisted of heating the dry gels at 10 °C min⁻¹, followed by an isothermal treatment at 700 °C for 3 h to obtain glassy powders.

2.3. Structure of the glasses

Some details of the short-range structure of the gel-derived glasses were revealed by Fourier transform infrared spectroscopy (FTIR), solid-state nuclear magnetic resonance (NMR) and high-resolution transmission electron microscopy (HR-TEM).

2.3.1. Fourier transform infrared spectroscopy (FTIR)

A Shimadzu 8400S spectrometer was employed for the FTIR analysis. The dried gel and glass powders were mixed with KBr powder and pressed into disks suitable for FTIR measurement. The FTIR spectra were recorded from 4000 cm⁻¹ to 400 cm⁻¹.

2.3.2. Nuclear magnetic resonance (NMR)

High-resolution ²⁹Si and ³¹P-NMR spectra were obtained using a Varian Unity INOVA spectrometer under a magnetic field of 9.4 T. For the ²⁹Si-NMR experiments, the samples were spun at 5 kHz in 7-mm zirconia rotors. Typical experimental parameters were: π/2-pulse durations of 3.3 μs, recycling delays of 150 s, and 600 scans were collected. For the ³¹P experiments, the samples were spun at 9 kHz in 4-mm silicon nitride rotors. Typical experimental parameters were: π/2-pulses of 2.0 μs, recycle delays of 1000 s, and 64 signals were collected. The chemical shift standards were a kaolinite sample for ²⁹Si (-91.5 ppm with respect to TMS) and 85% phosphoric acid solution for ³¹P (0 ppm).

2.3.3. High-resolution transmission electron microscopy (HR-TEM)

HR-TEM analyses were performed on a FEI TECNAI G² F20 microscope equipped with energy dispersive spectroscopy (EDS) for chemical analysis. The TEM specimens were prepared by putting one drop of 0.1% dispersed glass powders (< 10 μm) in acetone onto a TEM grid covered with carbon film and evaporating the solvent completely at room temperature.

2.4. Sintering and crystallization

The sintering and crystallization kinetics of the gel-glasses were evaluated by hot stage microscopy (HSM), differential scanning calorimetry (DSC) and X-ray diffraction (XRD). Based on the HSM and DSC results, isothermal heat treatments at different temperatures were designed to sinter and crystallize the glass powder compacts.

Table 1

Nominal composition of the glasses in mol%.

Sample	SiO ₂	CaO	P ₂ O ₅	ZrO ₂	K ₂ O
G	68	27	5	–	–
G–Zr	61.2	24.3	4.5	10	–
G–Zr–2K	61.2	22.3	4.5	10	2
G–Zr–4K	61.2	20.3	4.5	10	4
G–Zr–6K	61.2	18.3	4.5	10	6

2.4.1. Hot stage microscopy (HSM)

To identify the optimal temperature for sintering, the glasses were analyzed using a heating microscope (Misura HSM ODHT – Expert System Solutions). First, 30 mg of glass powder was manually pressed into a stainless steel mold at 25 MPa for 5 min. The sample (3 mm height \times 3.2 mm diameter) was placed on an alumina plaque and inserted inside the furnace. The measurement was performed at 10 °C/min up to 1400 °C. In the heating microscope, a light source was projected onto the sample, and a digital camera was used to capture the dimensional changes of its shadow.

2.4.2. Differential scanning calorimetry (DSC)

Differential scanning calorimetry tests were performed using a Netzsch DSC 404 instrument from 30 to 1100 °C at a rate of 10 °C min⁻¹ under air. For these experiments, 10 mg of glass for all the samples was placed in a covered platinum crucible.

2.4.3. X-ray diffraction (XRD)

Determination of the crystalline phases resulting from the heat treatments of glass samples was performed by XRD. We used a Rigaku Ultima IV X-ray diffractometer operating with CuK α radiation ($\lambda=0.15418$ nm). The diffraction patterns were obtained in the 2θ range from 15° to 80° in continuous mode at 0.02°/min.

The crystallized volume fractions, I_C , of the polycrystalline samples were roughly estimated using the procedure suggested by Krimm and Tobolsky [38]. I_C was estimated using the ratio of the crystalline area (A_C) of the peaks of the X-ray pattern of the polycrystalline specimens and the total area (A_T =crystalline+amorphous) of the same pattern using the following equation [38]:

$$I_C = \left(\frac{A_C}{A_T} \right) \times 100. \quad (1)$$

2.4.4. Isothermal heat treatments

The sintering and crystallization behavior was followed by firing glass pellets at various temperatures and calculating their relative density. Glass powder pellets (10 mm diameter and 3 mm high) were obtained by compacting 0.25 g of the powders in an uniaxial press at 65 MPa for 5 min. Then, the pellets were heated to sintering temperatures of 850, 950, 1000, 1100, 1200, and 1300 °C at a heating rate of 10 °C/min. Their relative densities were determined to follow the densification process. At least 5 specimens were used for each composition. The Archimedes method (immersion in water) was used to calculate the bulk density of the sintered compacts [39]. The true densities of the samples were estimated using a He displacement pycnometer (Quantachrome, Ultrapycnometer 1000), after crushing and milling the samples below 45 μ m. The bulk density was divided by the true density to calculate the relative density using the following equation [39]:

$$\rho_r = \frac{\rho_b}{\rho_t}, \quad (2)$$

where ρ_b is the bulk density, ρ_t is the true density and ρ_r is the relative density.

2.5. Microstructural observations

Scanning and high-resolution transmission electron microscopy (STEM and HR-TEM) as well as scanning electron microscopy (SEM) were performed to observe the shape and size of crystalline phases within the matrix of sintered glass-ceramics.

TEM was performed on a FEI TECNAI G² F20 microscope equipped with energy dispersive spectroscopy (EDS) for chemical analysis. The sample was prepared by placing one drop of 0.1 wt% dispersed glass-ceramic powders (< 10 μ m) in acetone onto a TEM grid covered with carbon film and evaporating the solvent completely at room temperature. Microstructural observations were performed using an FEI Magellan 400L electron scanning microscope coupled with an EDS analysis system. The experiments were performed on polished surfaces of the sintered samples etched for 40 s in a HF solution (1 wt%) and rinsed with acetone in an ultrasonic cleaner, dried and then coated by a thin film of gold for 1 min in a Quorum Q 150R machine.

2.6. Mechanical properties

Sintered and polished rectangular bars (2 mm \times 4 mm \times 30 mm) were used for three-point bending strength and fracture toughness measurements. These experiments were conducted in air at room temperature using an Instron Universal testing machine with a crosshead speed of 0.1 mm/min and a 20 mm span length between supports. At least five specimens were tested for each series of compositions based on the procedures described in the following subsections.

2.6.1. Three-point bending strength

The three-point bending strength (3-PBS) was calculated using the following formula:

$$3-PBS = \frac{3FL}{2bd^2}, \quad (3)$$

where F is the fracture force and b , d and L are the width, thickness and span length between supports (20 mm), respectively.

2.6.2. Fracture toughness

The fracture toughness was measured using two methods. First, the value was estimated using the microindentation method using Niihara's equation [40, 41]:

$$K_{IC} = \frac{g}{\phi} (Ha^{1/2}) \left(\frac{c}{a} \right)^{-3/2}, \quad (4)$$

where $g=0.48$ and $\phi=3$ are constants, H is the Vickers microhardness, a is the average value of the indentation half-diagonal, and c is the average value of the crack lengths measured from the center of each indent. At least 10

indentations were performed to calculate the average values for a and c in the polished specimens.

Then, the fracture toughness (K_{IC}) was measured for each sintered composition using the standard single-edge notch bending (SENB) technique [42,43]. For this test, the notch of a specimen was machined with a ~ 0.15 mm thick diamond saw disk. The saw depth was nearly half the width of the specimen. The specimens were fractured in a three-point bending fixture. The two halves of the broken specimens were used for the notch depth measurement under an optical microscope. The depth used was the average of five values at three locations of the notch: the middle and two sides of each section. The fracture toughness was calculated using the following formulas [42,43]:

$$K_{IC} = \frac{F_c}{d} \frac{L}{b^{3/2}} f\left(\frac{a}{b}\right)$$

$$f\left(\frac{a}{b}\right) = \frac{3(a/b)^{1/2}[1.99 - (a/b)(1 - a/b) \times (2.15 - 3.93a/b + 2.7a^2/b^2)]}{2(1 + 2a/b)(1 - a/b)^{3/2}}, \quad (5)$$

where F_c is the fracture force, d is the specimen thickness, b is the specimen width, L is the span length between supports (20 mm), a is the notch depth, and $f(a/b)$ is the stress intensity shape factor for brittle materials, which is calculated using the a and b values.

2.6.3. Microhardness

A Vickers microhardness tester (Equilam[®]) with a diamond pyramid indenter was used to measure the microhardness. The load was 500 g, and the loading time was 30 s. The hardness data were determined using at least ten indentations on each polished specimen.

2.7. In vitro bioactivity

To evaluate the bioactivity of the synthesized materials, *in vitro* tests were performed according to the method described by Kokubo et al. [44]. The simulated body fluid (SBF) used in this study was acellular and protein-free with a pH of 7.40. Table 2 lists the contents of this solution [44].

The *in vitro* bioactivity test was performed on sintered pellets with ~ 7 – 10 mm diameters and ~ 2 mm heights. Shortly after sintering, each pellet was fixed along its circumference by a nylon string to allow suspension in the SBF. The samples were first cleaned for 15 s in acetone and, after drying, were soaked in a polyethylene bottle containing the SBF. The same mass of

glass powder (0.25 g) was used to form the pellets for all the samples. Because the shrinkage and size of the pellets after sintering was different for each glass composition, the volume of SBF used in each bioactivity test was calculated according to the geometric area of each type of sample according to the procedure described by Kokubo et al. [44]:

$$V_s = \frac{S_a}{10}, \quad (6)$$

where V_s represents the volume of the SBF (mL) and S_a represents the total geometric area of the sample (mm²).

During the test, the samples were kept in contact with the SBF for 1, 3, 5, 7, 14 and 21 days, and the system temperature was maintained at 37 °C. After the time required for testing, each sample was removed from its bottle and immersed in acetone for 20 s for removal of the solution and to halt surface reactions. After drying, both sample surfaces were analyzed by FTIR and SEM to check for the formation of a superficial hydroxycarbonate apatite (HCA) layer.

2.7.1. FTIR analysis after bioactivity test

Monitoring of the pellet surface modifications after the *in vitro* bioactivity tests was performed via FTIR using a Bruker Tensor 27 spectrometer operating in reflectance mode with a 4 cm⁻¹ resolution in the 4000–400 cm⁻¹ region.

2.7.2. Surface observations by SEM

Morphological characterization of the pellets with respect to the surface modifications after the *in vitro* bioactivity test was performed using SEM. A set of samples was selected and analyzed before and after soaking in SBF at various testing times. The samples were coated with a thin gold layer and analyzed under a FEI Inspect S50 microscope coupled with an energy dispersive X-ray spectroscopic analysis system (EDS), which aided surface characterization through qualitative chemical analysis.

2.7.3. pH measurement

Immediately after removal of the samples from the SBF, the pH of the medium was measured at least for three series of the test.

3. Results and discussions

3.1. Vitrification of the dried gels

It is well documented that upon sufficient heat treatment of dried gels, the volatile ingredients and sub-products resulting from the sol–gel processing can be eliminated, and the gel can be converted into a glass; however, in most cases, crystallization occurs (and crystallization must be avoided to obtain a glass) [6–14]. To understand this process, simultaneous DTA/TG and XRD analyses were performed to identify the critical temperatures for converting the dried gels into glasses. The results of the DTA-TG analyses of the dried gels are presented in Fig. 1a–e.

Our gels underwent three distinct mass losses and become practically stable at approximately 700 °C. The first mass loss

Table 2

Ionic concentration of SBF used for evaluation of *in vitro* bioactivity [44,45].

Simulated body fluid (SBF)	Ionic concentration (mmol L ⁻¹)							
ISO 23317 (June 2007)	Na ⁺	K ⁺	Mg ²⁺	Ca ²⁺	Cl ⁻	HCO ₃ ⁻	HPO ₄ ²⁻	SO ₄ ²⁻
SBF ^a	142.0	5.0	1.5	2.5	147.8	4.2	1.0	0.5

^aBuffer: tris(hydroxymethyl)aminomethane (TRIS).

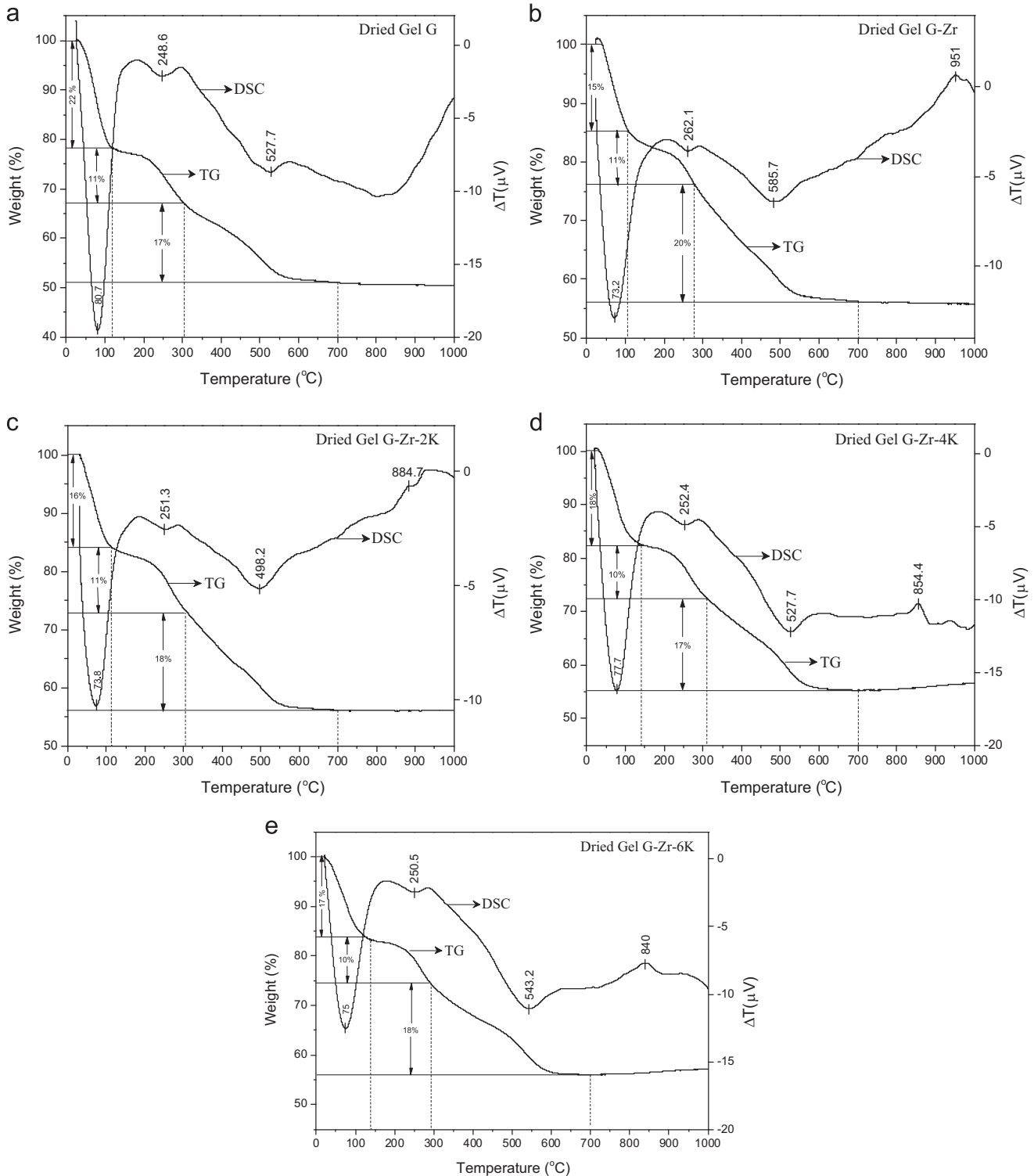


Fig. 1. DTA and TG curves for dried gels.

step occurred at ~ 25 – 100 °C and is associated with the endothermic process of desorption of physically adsorbed water and alcohol at ~ 70 – 80 °C [14–17,37]. The second mass loss step occurred near 250 °C and is related to the volatilization of water, an endothermic chemical desorption process. The third mass loss stage was more pronounced. This stage is attributed to the evolution of the resulting sub-products

from incomplete condensation of the precursors, mostly elimination of the nitrate ions originating from $\text{Ca}(\text{NO}_3)_2 \cdot 4\text{H}_2\text{O}$, KNO_3 and $\text{ZrO}(\text{NO}_3)_2 \cdot \text{XH}_2\text{O}$ [17,37]. Further weight loss due to the nitrate decomposition in the sample containing Zr could be related to the substitution of zirconium oxynitrate for TEOS and TEP (when Zr-oxynitrate replaces TEOS and TEP, additional weight loss of nitrate is observed).

However, it is clear that substitution of KNO_3 for $\text{Ca}(\text{NO}_3)_2$ results in less mass loss in the third stage (from 20% to $\sim 18\%$) because of the one mole decrease in the nitrate content. The exothermic peaks located between 850°C and 950°C are associated with the onset of crystallization.

Based on the DTA and TG analyses, the stabilization temperature used here to convert the dried gels into glasses was set at 700°C . Treatment for 3 h was considered sufficient for complete elimination of the nitrate ions. Furthermore, this condition also allowed the possibility of obtaining glassy materials because crystallization was only observed in DTA runs between ~ 850 and 950°C .

According to the X-ray diffractograms presented in Fig. 2, all the samples appear to be non-crystalline. However, the diffraction pattern of sample G exhibits one reflection centered at $2\theta = 32^\circ$. A very weak peak also appears for G-Zr. This peak can be attributed to apatite, which will be confirmed by NMR and HR-TEM analyses in the next section.

3.2. Structure of the glasses

To elucidate the properties of the glasses, it is fundamental to have a good understanding of their structure. For example, in most cases, the structure of silicate-based bioactive glasses consists of a covalent-bonded network of SiO_2 , which is the main network former, together with P_2O_5 . Both $[\text{SiO}_4]^{4-}$ and $[\text{PO}_4]^{3-}$ tetrahedral units are covalently bonded through bridging oxygen atoms at the corners. CaO , Na_2O and K_2O are network modifiers. Ca^{2+} , Na^+ and K^+ cations disrupt the covalent network and produce non-bridging oxygen atoms. Whereas network formers provide stability, network modifiers increase the glass reactivity and, therefore, the bioactivity [2,3].

In sol-gel glasses, especially in the SiO_2 - CaO - P_2O_5 system, the tetrahedral $[\text{SiO}_4]^{4-}$ units condensate as connected branches of 3 or more $[\text{SiO}_4]^{4-}$ membered rings, depending on the stabilization temperature [8,46–48]. CaO is a network modifier [46–48]. The role of P_2O_5 in these glasses is more complex [49].

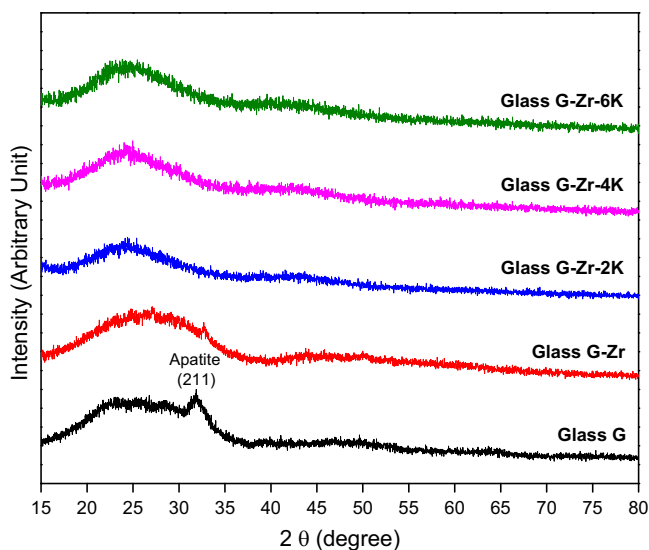


Fig. 2. XRD patterns of glasses heat-treated at 700°C for 3 h.

In fact, amounts over 10 mol% of this component lead to non-bioactive compositions [50], whereas some P_2O_5 -free SiO_2 - CaO sol-gel glasses are bioactive [51,52]. It has been demonstrated by high-resolution transmission electron microscopy (HR-TEM) and solid ^{31}P -nuclear magnetic resonance (NMR) spectroscopy that orthophosphate nano-crystals appear after conversion of the gel to glass in SiO_2 - CaO - P_2O_5 glasses [8,53–55]. These non-soluble segregated nano-crystals normally decrease the Ca-H^+ ionic exchange but facilitate hydroxyapatite (HA) formation because a new amorphous calcium phosphate is previously formed on the glass surface [53–55]. As briefly described above, the structure of gel-derived SiO_2 - CaO - P_2O_5 has been investigated previously. Therefore, hereafter, we intend to reveal the consequence of ZrO_2 and K_2O addition on the structure of these glasses.

The FTIR spectra obtained from dried gels and glasses are presented in Fig. 3a and b, respectively. For the dried gels (Fig. 3a), the high-frequency broad band at approximately 3400 cm^{-1} is due to the symmetric stretching of the OH group. The band at $\sim 1600\text{ cm}^{-1}$ is assigned to the deformation vibration of the H-O-H bond. There is another band at $\sim 1384\text{ cm}^{-1}$, which is attributed to the NO_3^- groups' vibration. The absorption bands at approximately 1200, 1060, 800 and 460 cm^{-1} are all characterized by silicon-oxygen bonds. The bands at 1200 and 1060 cm^{-1} are assigned to the LO and TO modes of the Si-O-Si asymmetric bond stretching vibration, respectively. The bands at 800 cm^{-1} and 460 cm^{-1} are associated with Si-O-Si symmetric stretching and bending vibrations, respectively. The fact that these absorption bands appear in the gels dried at low temperature (150°C) confirms the formation of the silicon-oxygen anionic network structure in the gels. The transmittance at 950 cm^{-1} , the intensity of which significantly increases (absorbance decreases) with the addition of ZrO_2 , is associated with the vibration of Si-NBO bonds (NBO=non-bridging oxygen). Two weak bands at approximately 740 and 790 cm^{-1} are associated with the vibration of single or double bonds of P-O in the $[\text{PO}_4]^{3-}$ group [8–15]. When ZrO_2 is added to the base gel, one clear distinction appeared in the FTIR spectra, and the intensity for Si-NBO considerably decreased. There are no notable changes in the FTIR spectra of the dried gels as a result of the addition of K_2O .

The FTIR spectra for the glasses (obtained by heating dried gels at 700°C for 3 h) are presented in Fig. 3b. Similar to the dried gels, the 3400 cm^{-1} and 1600 cm^{-1} vibration bands are attributed to H-O-H and O-H bonds, respectively. The band at $\sim 1384\text{ cm}^{-1}$ attributed to the NO_3^- groups disappeared in the glasses because of the decomposition of nitrate groups after stabilization. Additionally, four spectra are characterized by the presence of bands at approximately 1200, 1060, 800 and 460 cm^{-1} , which are associated with stretching vibration and bending vibration of Si-O-Si bonds. The double peaks at 570 and 600 cm^{-1} are associated with the P-O bending mode related to the presence of crystalline phosphate in the glass [8–15].

By comparing the FTIR spectra of the glasses, three main differences were identified. First, it appears that ZrO_2 diminishes the intensity of the Si-NBO band at $\sim 950\text{ cm}^{-1}$ with broadening of the 1060 cm^{-1} (Si-O-Si) band. Second,

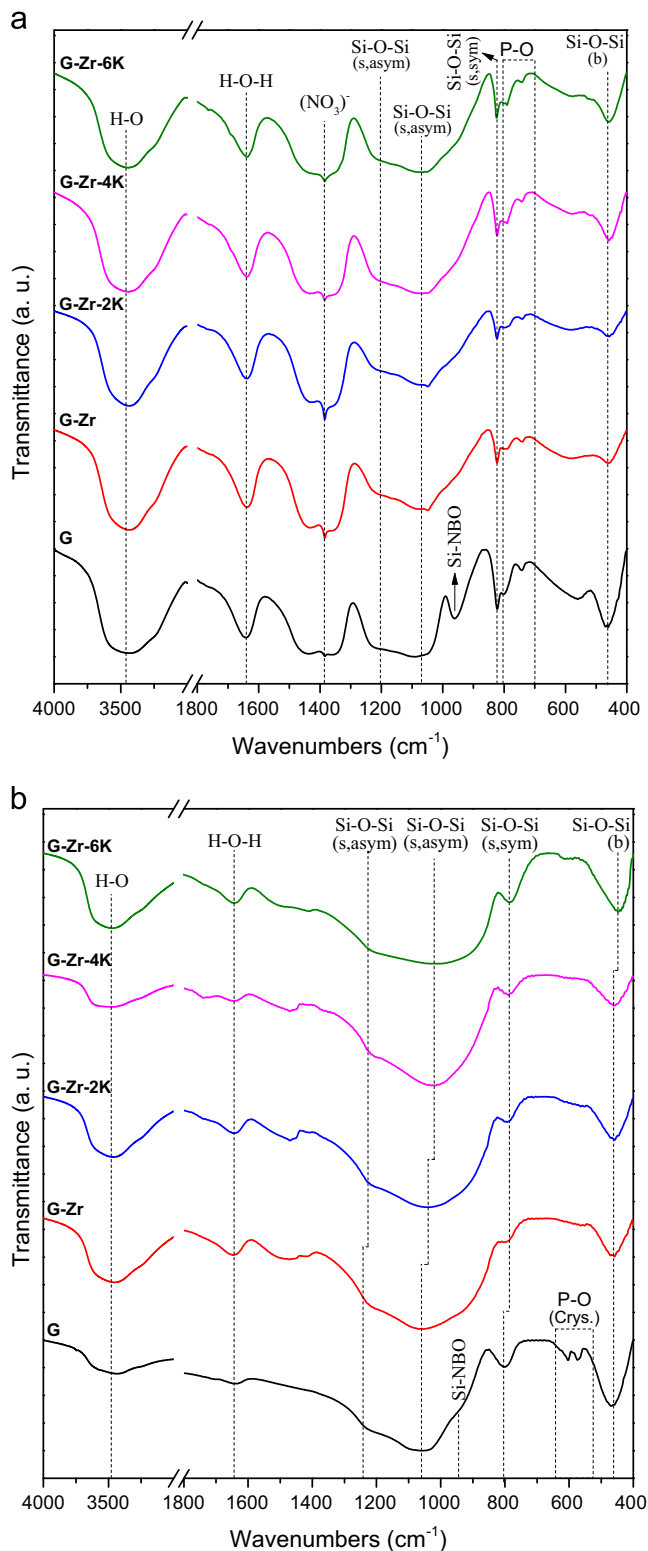


Fig. 3. FTIR spectra of (a) dried gels and (b) glasses.

no P–O vibration due to the presence of crystalline phosphate was observed in the zirconium containing glasses. Finally, the potassium addition shifted the Si–O–Si vibration bands to lower wavenumbers (lower energy). IR frequency shifting of the bridging oxygen stretching vibration Si–O–Si is known to

be caused by the increased content of alkaline modifiers, *e.g.*, K^+ with lower ionic field strength than Ca^{2+} [56].

To further elucidate the structure of the glasses and better understand the role of ZrO_2 incorporation, ^{29}Si -NMR and ^{31}P -NMR analyses were also performed on selected samples. The ^{29}Si -NMR spectra from glasses G and G–Zr and samples containing 2 and 6 mol% K_2O are presented in Fig. 4a. These spectra reveal well-resolved resonances from Q^4 and Q^3 tetrahedra in addition to partially resolved Q^2 and Q^1 . The Gaussian least-square fittings to these spectra yield the silicon fractions $I(Q^n)$ for these species, as shown in Table 3 along with ^{29}Si isotropic shifts. The average number of Si–O–Si bridges per tetrahedron (BO), which quantifies the degree of Si–O–Si connectivity of a silicate network, was calculated based on these silicon fractions using the following expression:

$$BO = \sum_{n=1}^4 n I(Q^n). \quad (7)$$

For the sample G–Zr–6K, the overlap between the resonances precludes any quantitative analysis of the spectrum. For glasses containing K_2O , there is a systematic shift of the resonances to higher frequencies. This trend can be observed even in the less resolved spectrum of G–Zr–6K through the variation of the average isotropic shift of the spectra observed in Table 3. These ^{29}Si deviations are consistent with similar observations reported in the literature [57] and can be explained by the incorporation of K^+ at the expense of Ca^{2+} interacting with a non-bridging O in these glasses. As K^+ has a smaller ionic potential compared with Ca^{2+} , the isotropic shifts of Q^n groups with non-bridging oxygens (NBOs) coordinated to K^+ will have higher resonance frequencies than similar groups with all the NBOs coordinated with Ca^{2+} [57]. This effect was also identified by FTIR spectroscopy, where the Si–O–Si stretching vibration bands shifted to lower wavenumbers with the addition of K. Therefore, the expected role of K^+ as a modifier was confirmed.

The comparison of the population of Q^n species and the average number of bridging oxygens per tetrahedron between glasses G and G–Zr indicates a decrease in the average connectivity of the Si–O–Si network in the glass containing ZrO_2 . This result indicates that Zr^{4+} ions are at least partially entering the glass network.

Because we observed a clear difference in the intensity of Si–NBO in the FTIR spectra of the dried gels G and G–Zr (Fig. 3a), we decided to perform a ^{29}Si -NMR analysis of the dried gels as well. The ^{29}Si -NMR spectra of the dried gels G and G–Zr are presented in Fig. 4b. The relative intensity of the Q^n species, average numbers of Si–O–Si bridging oxygens and average chemical shifts are presented in Table 3.

Upon heating the dried gels at 700 °C, the average connectivity of the silicate network decreases from 3.6 to 3.3 for G (the conversion of the dried gel G to glass G) and from 3.5 to 3.0 for G–Zr (the conversion of the dried gel G–Zr to glass G–Zr). This behavior is due to the well-known role of calcium as a modifier in gel-derived glasses, as confirmed by Lin et al. [47]. These researchers demonstrated that Ca is incorporated

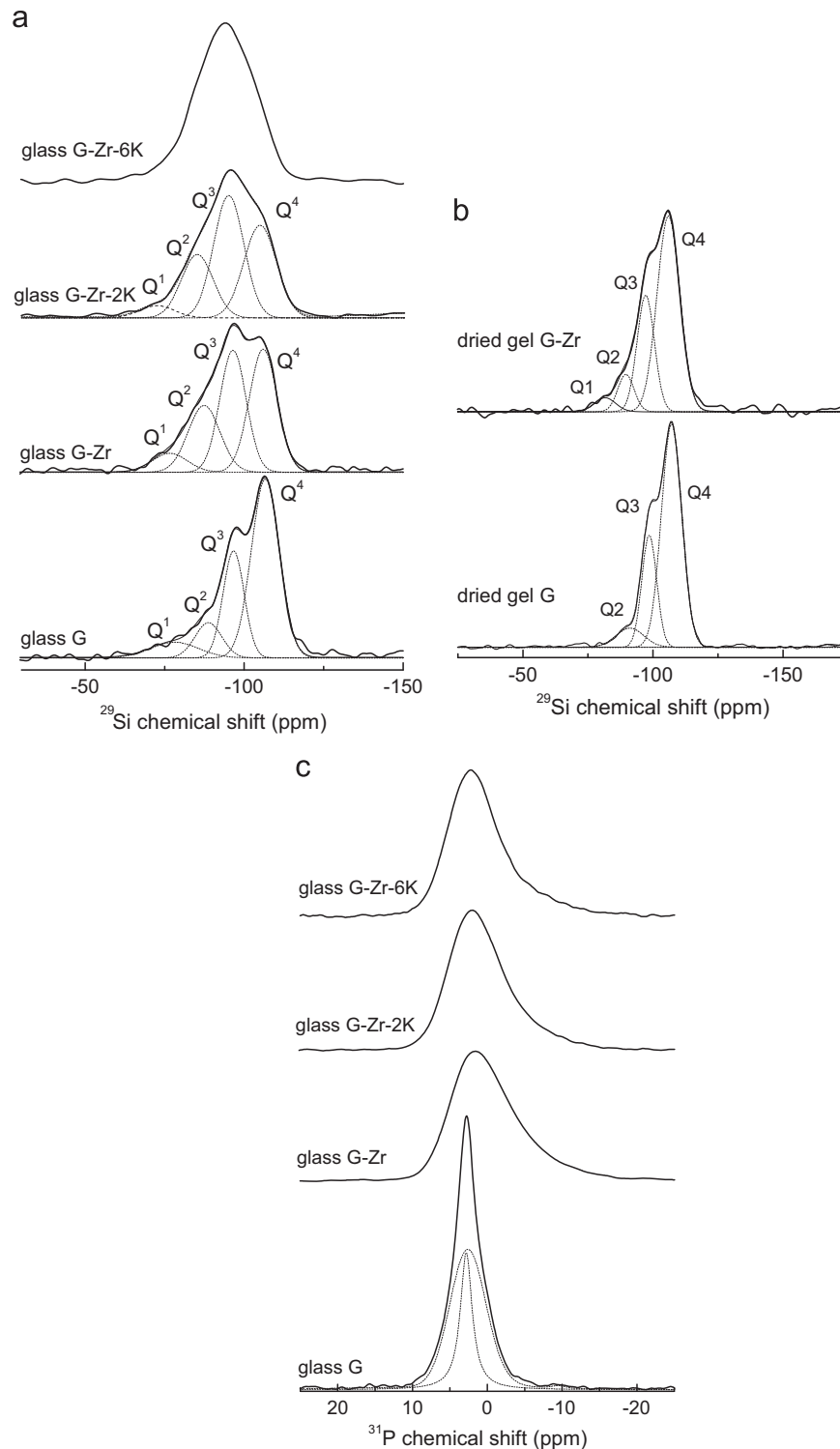


Fig. 4. (a) ^{29}Si -NMR spectra of glasses, (b) ^{29}Si -NMR spectra of dried gels G and G-Zr (c) ^{31}P -NMR spectra of glasses. Dotted lines: least-square fittings.

into the network after decomposition of calcium nitrate at temperatures above 400 °C, which significantly decreases the silica network connectivity [47].

It is also evident from Fig. 4a and b as well as Table 3 that Zr incorporation decreases the Si–O–Si connectivity of both gels and glasses, whereas the role of K and Ca as modifiers is

clear. Two hypotheses, described below, are expected for the role of Zr:

- (i). *Zr as modifier*: as the O/Si ratio in glass G–Zr increases with respect to G, there could be some breakage of Si–O–Si bridges leading to smaller average connectivity of the

Table 3
Fractions of silicon species Q^n in our glasses obtained from least-square fittings of the ^{29}Si -NMR spectra. Estimated uncertainty: $\pm 10\%$. BO: average number of bridging oxygen per silicate tetrahedron. δ and I represent the ^{29}Si chemical shift and relative intensity. δ_{CG} : average isotropic chemical shift of the ^{29}Si -NMR spectra.

Sample	Q^4		Q^3		Q^2		Q^1		BO	δ_{CG} (ppm)
	I	δ (ppm)	I	δ (ppm)	I	δ (ppm)	I	δ (ppm)		
Glass G	0.56	-106.7	0.27	-96.6	0.11	-88.1	0.06	-76.9	3.3	-99.9
Glass G-Zr	0.36	-106.0	0.34	-96.5	0.23	-87.4	0.07	-76.6	3.0	-96.2
Glass G-Zr-2K	0.33	-105.0	0.40	-95.2	0.22	-85.2	0.05	-72.6	3.0	-94.8
^a Glass G-Zr-6K	–	–	–	–	–	–	–	–	–	-93.6
Dried Gel G	0.67	-107.2	0.25	-98.6	(0.08) ^b	-91.2	–	–	(3.6) ^c	-103.9
Dried Gel G-Zr	0.61	-106.0	0.27	-97.2	(0.12) ^b	-89.6	–	-81.7	(3.5) ^c	-101.6

^aDeconvolution was not possible due to lack of resolution of the Q^n resonances.

^b Q^2+Q^1 .

^cLess reliable, due to poor separation of Q^2 and Q^1 .

silicate network. This phenomenon leads to a decrease of BO and an increase of NBO. However, we observed a significant reduction in the number of NBOs in the FTIR spectra of the dried gels after the incorporation of Zr. This reduction was also visible in the FTIR spectra of the glasses, but with lower resolution. Therefore, this observation questions the role of Zr as a modifier.

- (ii). *Zr as glass former*: Zr may indeed act as a glass former with $[\text{ZrO}_4]^{4-}$ units occupying some positions of $[\text{SiO}_4]^{4-}$ tetrahedra. The amount of shift of the ^{29}Si resonance for a given tetrahedron due to each covalent Si–O–Zr bridge is positive [58] and is below 5 ppm (which is also the well-known shift caused by, e.g., a Si–O–Al bridge: almost half the separation of Q^n and Q^{n-1}) [57,58]. Therefore, it is not likely that, for example, the resonance of a Q^4 with one Si–O–Zr bridge might fall over a Q^3 resonance; however, this scenario may occur for a Q^4 resonance with two Si–O–Zr. Therefore, the number of Q^4 decreases in favor of an apparent increase in Q^3 . However, we cannot identify with certainty the occurrence of this process from the spectra because of the broadening of the resonances. It is not possible to predict how these $[\text{ZrO}_4]^{4-}$ substitutions will affect the fitted areas for nominal Q^4 or Q^3 . There is also the possibility that $[\text{ZrO}_4]^{4-}$ will bond to Q^1 , Q^2 or Q^3 , linking two or more $[\text{SiO}_4]^{4-}$, without perturbing the average number of BOs of the Si–O–Si network. In this case, the apparent connectivity of the silicate network would be invariant.

Therefore, we cannot find strong evidence for or against the role of Zr as a network former based on the NMR analysis. However, it would be more consistent to consider Zr as a glass former because the FTIR analysis shows that Zr addition decreases the average number of non-bridging oxygens. Additionally, we have demonstrated that in our glasses, Zr leads to a very low solubility in SBF, indicating its stabilization of the glass structure [37].

The role of Zr as a network former has been demonstrated by numerous scientists, e.g., [59,60], who worked on the

synthesis and characterization of SiO_2 - ZrO_2 refractory materials using the sol-gel method. These researchers demonstrated that Zr ions are indeed incorporated into the silica network [58–60].

Fig. 4c present the ^{31}P -NMR spectra for glasses G, G-Zr, G-Zr-2K and G-Zr-6K. Glass G exhibits a spectrum composed of two overlapping components: a broad one centered at 2.5 ppm and a narrower Lorentz-like component centered at 2.8 ppm. According to the central chemical shift of these resonances, they can be attributed to Q^0 tetrahedra interacting with Ca^{2+} . Lorentz-like line-shapes for the NMR resonances are not expected in glasses but in crystalline materials. Therefore, it can be concluded that glass G exhibits some degree of crystallization of a Ca-phosphate phase, confirmed by FTIR (Fig. 3b). The XRD pattern reveals a very small peak at $2\theta=32^\circ$ (Fig. 2), and a small piece of glass after heat treatment at 700°C is white and opaque.

The ^{31}P chemical shift of the narrow resonance line agrees with the value observed for apatite (2.9–3.3 ppm) [61]. The presence of apatite was also observed in an HR-TEM image. Fig. 5 presents the HR-TEM image obtained from sample G after a 3 h heat treatment at 700°C . This image reveals two d-spaces at 0.28 and 0.21 nm, which can be assigned to (211) and (302) reflections of an apatite crystal, respectively.

Fig. 4c also presents the ^{31}P -NMR spectra for glasses containing Zr. The spectrum for glass G-Zr reveals a main resonance, with a maximum at 1.7 ppm. This chemical shift can be attributed to Q^0 groups associated with Ca^{2+} . The low-frequency shoulder of the spectrum indicates the presence of some Q^1 groups associated with Ca^{2+} and/or Q^0 associated with Zr^{4+} . The substitution of Zr^{4+} ions for Ca^{2+} near the $[\text{PO}_4]^{3-}$ units may diminish the affinity for apatite formation. In other words, Zr^{4+} with a higher ionic field strength will interact with the phosphate group and push the Ca^{2+} aside, which is the main cause stopping apatite formation and obtaining completely amorphous glasses in samples containing ZrO_2 . The amorphous nature of these glasses was previously demonstrated by XRD and FTIR analyses (Figs. 2 and 3b).

The spectra (Fig. 4c) for G-Zr-2K and G-Zr-6K are similar to that of G-Zr, with only a slight shift to higher frequencies

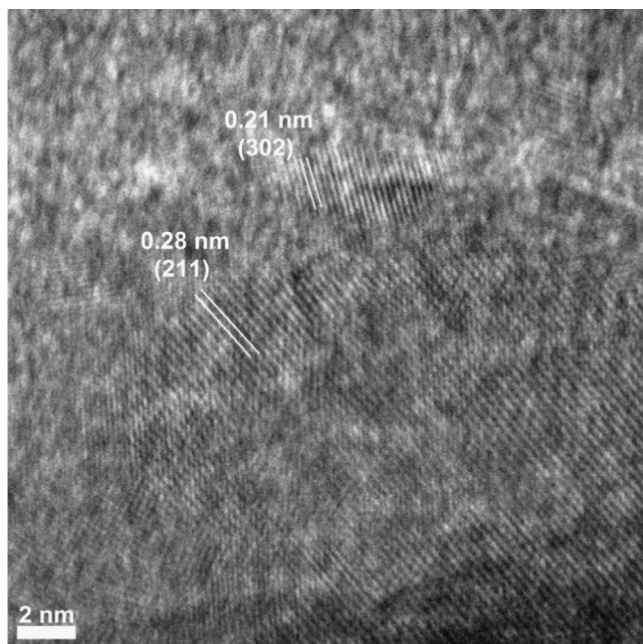


Fig. 5. HR-TEM image of sample G after 3 h heat treatment at 700 °C.

(with a maximum at 2.2 ppm for sample G–Zr–6K), indicating the presence of K^+ near some of the Q^0 and Q^1 phosphates. The resonances appear narrower, an effect that is also expected if K^+ , with a smaller ionic potential, is replacing some Ca^{2+} or Zr^{4+} associated with non-bridging oxygens from the phosphate groups.

3.3. Sintering and crystallization

The shrinkage of the glass powder compacts with increasing temperature obtained by hot stage microscope is shown in Fig. 6a. Rapid shrinkage started for all the compositions at approximately 800 °C and stagnated at approximately 950 °C, 930 °C, 895 °C, 880 °C and 857 °C for glasses G, G–Zr, G–Zr–2K, G–Zr–4K and G–Zr–6K, respectively. Glasses G and G–Zr started to shrink again after 1050 °C and 1300 °C, respectively, up to the end of the thermal cycle. The glasses that contained K_2O continued to shrink after a very short stagnant interval (~ 70 °C) and reached their maximum shrinkage at approximately 1100 °C, 1090 °C and 1050 °C for G–Zr–2K, G–Zr–4K and G–Zr–6K, respectively. Then, these samples slightly expanded and finally softened into a spherical shape.

Fig. 6b presents the DSC curves of all the glasses. In this Figure, the crystallization temperatures are illustrated. A comparison between the HSM and DSC curves reveals that the temperatures at which the shrinkage became stagnant correspond to the crystallization temperatures. Therefore, it is apparent that crystallization stops the (viscous) sintering progress. This effect is more evident for samples G and G–Zr, which exhibit sharp crystallization peaks between 920 and 1030 °C. However, the K_2O -containing samples are more resistant to devitrification and achieve their maximum shrinkage before the softening points.

The relative densities of the samples isothermally sintered at various temperatures for 3 h are shown in Fig. 6c. The changes in the relative density are very similar to the shrinkage variations. Samples G and G–Zr reached their maximum density at around 1300 °C. However, samples G–Zr–2k, G–Zr–4K and G–Zr–3K almost reached their highest densities at 1050 °C, 1025 °C and 1000 °C, respectively.

It is clear that substitution of K_2O for CaO in sample G–Zr considerably improved its sinterability. The maximum density for sample G–Zr at 1300 °C was approximately 87%, whereas the addition of only 2 mol% K_2O increased it up to 94% at a much lower temperature (1050 °C). The DSC curves reveal that the K_2O addition reduces the tendency of crystallization such that the sample with 6 mol% K_2O does not exhibit a distinct crystallization peak.

Fig. 7a and b present the XRD patterns of samples G and G–Zr heat treated at various temperatures, respectively. Sample G exhibits one reflection centered at $2\theta = 32^\circ$ that corresponds to the crystallization of apatite at 850 °C. This sample heated between 950 °C and 1200 °C revealed maxima that matched to β -wollastonite and apatite. At 1300 °C, the wollastonite transformed to pseudo-wollastonite, and a sharp maximum appeared at $2\theta = 22^\circ$, which was attributed to cristobalite.

The XRD pattern of sample G–Zr (Fig. 7b) at 850 °C is characteristic of an amorphous material, and no crystalline phases were detected. The sample heated between 950 °C and 1000 °C contained apatite, wollastonite and tetragonal-zirconia phases. Upon heat treatment at higher temperatures (1100 °C and 1200 °C), the zirconia and wollastonite gradually transformed into zirconium silicate (zircon) and pseudo-wollastonite, respectively. Finally, cristobalite appeared at 1300 °C.

Fig. 7-c presents the XRD patterns of sintered samples with various K_2O contents. These samples remained almost amorphous up to 850 °C. After sintering at 1050 °C and 1025 °C, the apatite–zirconia crystallized in samples G–Zr–2K and G–Zr–4K, respectively. However, the apatite was the only phase appearing in sample G–Zr–6K after heat treatment at 1000 °C.

A comparison between the DSC (Fig. 6) and XRD (Fig. 7) results indicates that the exothermic peaks observed in the DSC traces at approximately 930 °C and 1027 °C for samples G and G–Zr are related to the crystallization of apatite and zirconia, respectively. The very small crystallization peak appearing in the DSC curves of samples containing K_2O is related to the crystallization of apatite. Additionally, it appears that K_2O addition significantly postpones the crystallization of apatite in a manner that at 1000 °C, only a small amount of apatite crystallized in G–Zr–6K.

3.4. Microstructure

The HR-TEM images obtained from glasses G and G–Zr sintered at 1000 °C for 3 h are presented in Fig. 8a and b, respectively. These images reveal a glassy matrix containing crystalline domains. The size of the crystalline spheres in sample G is around 70 nm, with an interplanar spacing close to 0.21 nm. The crystalline size in sample G–Zr is smaller (~ 5 nm), and two d-values of 0.21 nm and 0.25 nm are

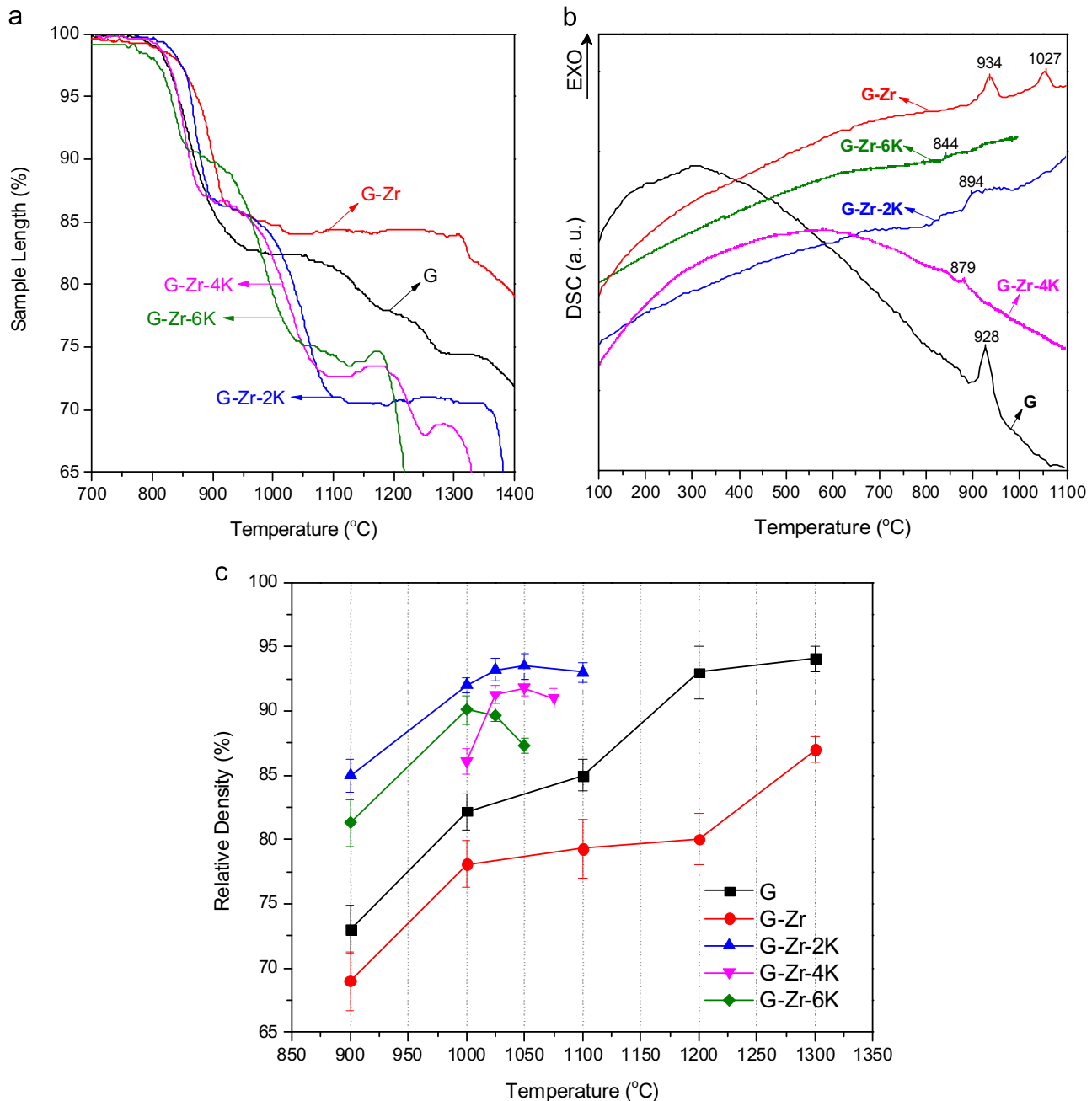


Fig. 6. (a) Reduction in sample length (shrinkage) versus temperature, (b) DSC curves for glasses showing the crystallization temperatures and (c) relative density of samples sintered at different temperatures.

observed. The d-value of 0.21 nm in both samples can be attributed to (302) planes of nanocrystalline apatite, which were also observed in the base glass heated at 700 °C (Fig. 5). The d-spacing of 0.25 nm may be related to the presence of nanocrystalline zirconia, which exhibits a reflection at $2\theta=35.6^\circ$ with a d-value of 0.25 nm corresponding to (200) planes (JCPDS 2-0733).

A scanning transmission electron microscope image captured near the edge of the G-Zr glass-ceramic powder particles is presented in Fig. 9. In this image, dark spherical particles are distributed in a bright matrix. The EDS analysis performed on these particles (point 1) revealed the presence of Zr, Si and Ca.

However, the matrix (point 2) is rich in Si, P and Ca. It appears that these spherical particles with an average size of 20–30 nm are zirconia particles.

Back-scattered SEM micrographs of the sintered specimens containing 2–6 mol% K_2O etched with 1 wt% HF solution for 40 s are presented in Fig. 10a–f. The microstructure of these samples consists of a black and gray matrix. The HF acid attacks the silica-rich glassy regions and dissolves them, leaving a black area. The gray areas, which are very similar to the dendritic growth of a crystalline phase, can be attributed to the presence of apatite or a Ca/P-rich region. In the G-Zr-2K and G-Zr-4K glass-ceramics, white and very fine spherical particles were

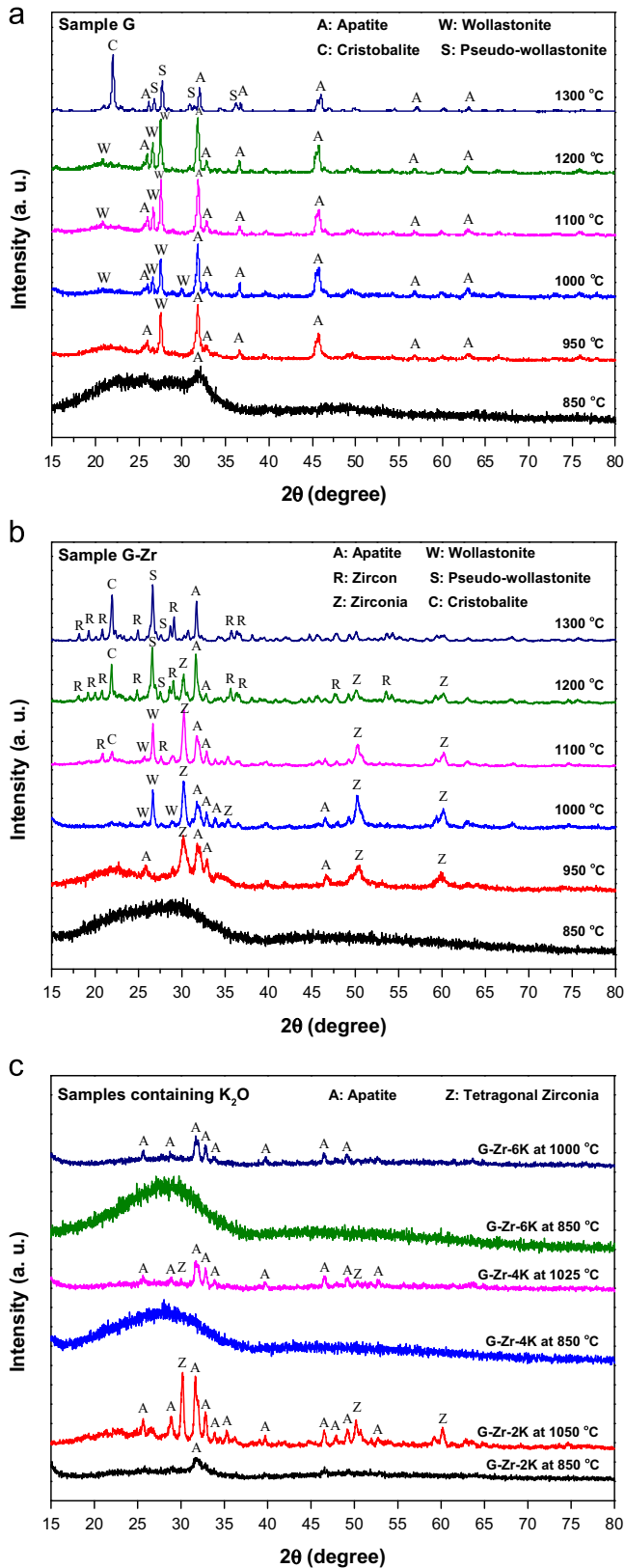


Fig. 7. XRD patterns of samples (a) G, (b) G-Zr and (c) containing K_2O heat treated in various temperatures for 3 h.

detected (Fig. 10b and d). These particles are uniformly dispersed in the matrix and have average particle sizes of ~ 55 – 65 nm. The brighter particles in the back-scattered SEM image confirm the presence of a heavy element such as zirconium, which back-scatters electrons stronger than light elements such as Si, Ca, P and K. Therefore, these particles can be considered to be zirconia, and its crystallization was confirmed previously by XRD and DSC. The amount of zirconia crystals in the G-Zr-2K sample is higher than that in the G-Zr-4K sample. Finally, there is no evidence of crystallization of zirconia in the G-Zr-6K glass-ceramic. Additionally, more significant dissolution of the glassy matrix in HF etchant can be observed, indicating a higher content of the glassy phase in this sample.

3.5. Mechanical properties

Based on the sintering and crystallization behavior of the investigated glasses, some sintered samples were selected for evaluation of the mechanical and biological properties. For compositions G and G-Zr, maximum densification was only achieved at approximately 1300 °C. Zirconia started to react with the residual glass at 1100 °C, and zirconium silicate (zircon) was formed (Fig. 7b). Cristobalite appeared in these samples at approximately 1100 °C. At 1300 °C, apatite, pseudo-wollastonite, zirconium silicate (zircon) and cristobalite were identified (Fig. 7a and b).

Zirconium silicate is insoluble in aqueous media similar to ZrO_2 [24–30]. Wollastonite is soluble and bioactive; however, its high-temperature polymorph pseudo-wollastonite is less soluble [62–64]. Cristobalite leads to matrix cracking during cooling and degradation of bioactivity [14,15,62,63]. It seems that these “inert” phases are neither good for bioactivity nor for mechanical properties. In addition, densification for sample G-Zr almost stopped at around 1000 °C because of crystallization (Fig. 6c). Therefore, we decided to focus on samples G and G-Zr, which were sintered at 1000 °C for further investigation. Although these specimens were not fully densified, they contained suitable crystalline phases, such as apatite, wollastonite and nano-sized tetragonal zirconia, which, in principle, could improve the bioactivity and, simultaneously, the mechanical properties. The glass-ceramics G-Zr-2K, G-Zr-4K and G-Zr-6K sintered at 1050 °C, 1025 °C and 1000 °C, respectively, were also selected. These samples contained apatite and nano-sized zirconia crystals (Fig. 10).

The mechanical properties, relative density and crystalline volume fraction of the sintered specimens are summarized in Table 4. G and G-Zr sintered to almost 82% and 78% of their true density, respectively. Samples G-Zr-2K, G-Zr-4K and G-Zr-6K showed the maximum relative densities of 94%, 91% and 90%, respectively.

The crystal volume fraction in sample G-Zr was the highest. K_2O addition retarded crystallization and increased the amount of residual glass.

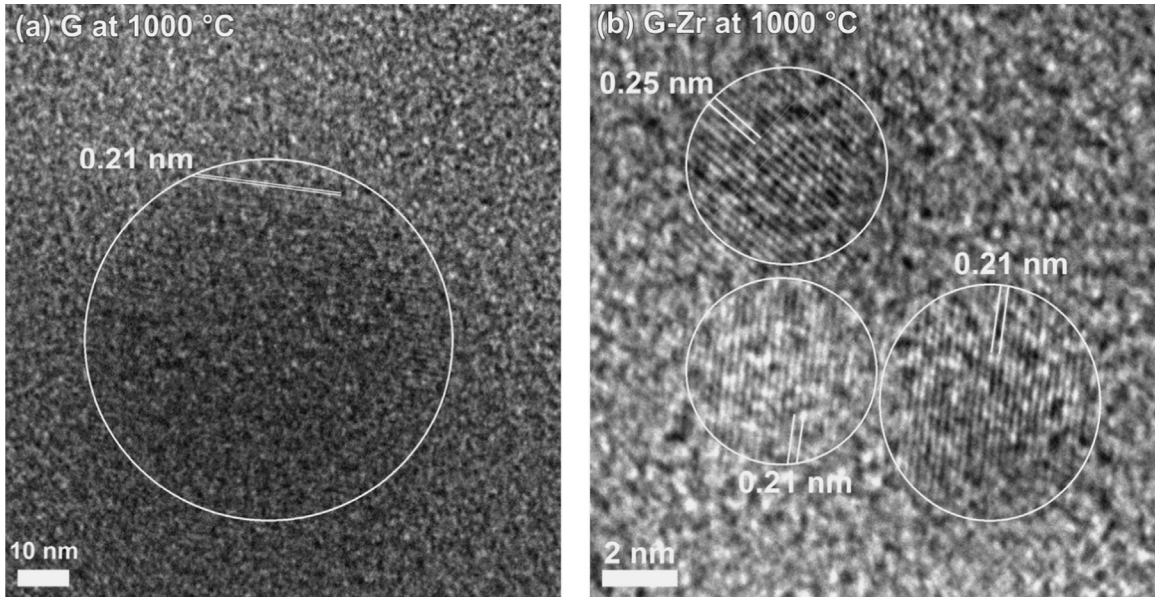


Fig. 8. HR-TEM images obtained from the glass-ceramic powders G and G-Zr ($< 10 \mu\text{m}$) heat treated at $1000 \text{ }^\circ\text{C}$ for 3 h.

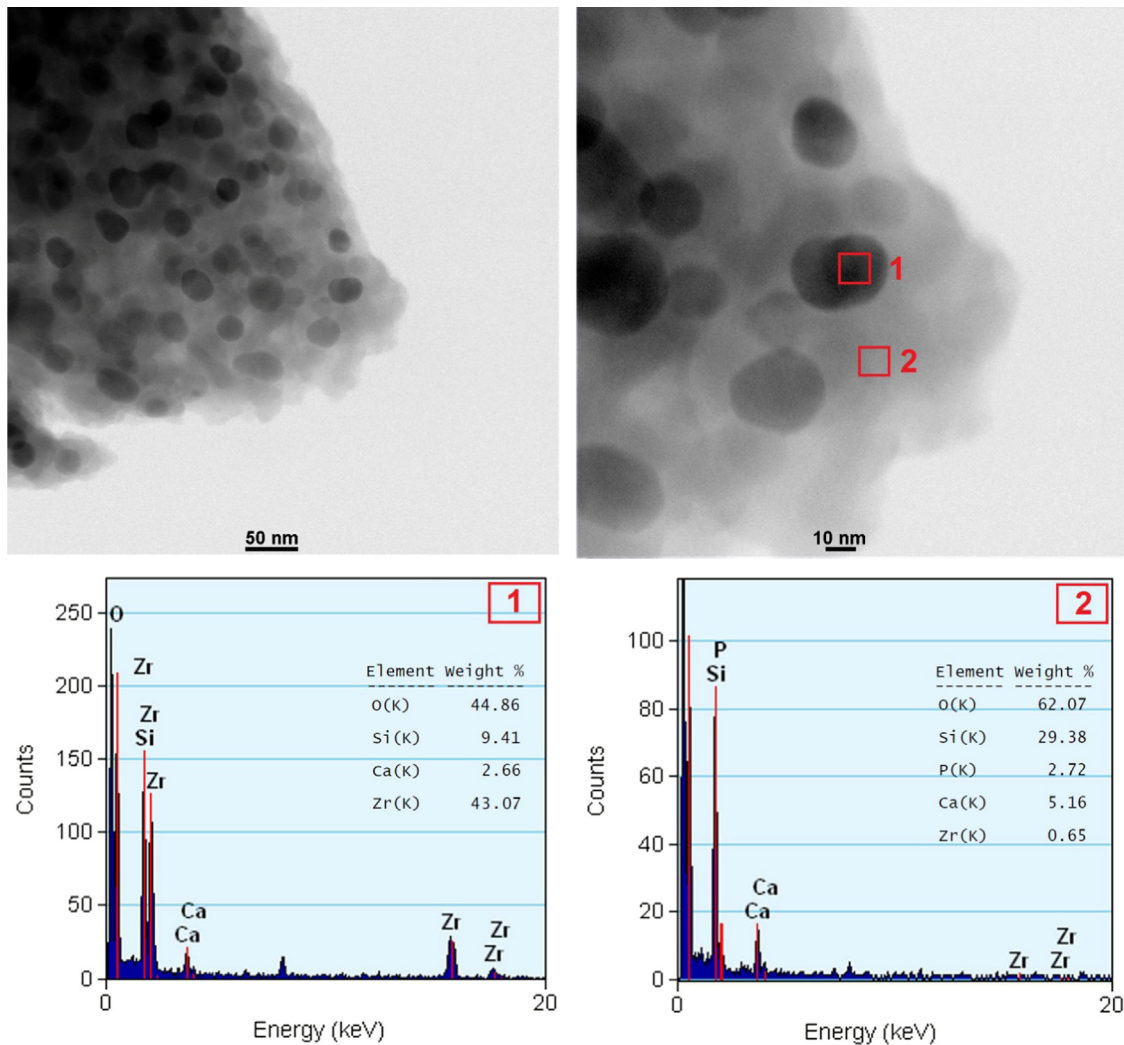


Fig. 9. Scanning electron transmission microscope image obtained from the glass-ceramic G-Zr sintered at $1000 \text{ }^\circ\text{C}$ for 3 h.

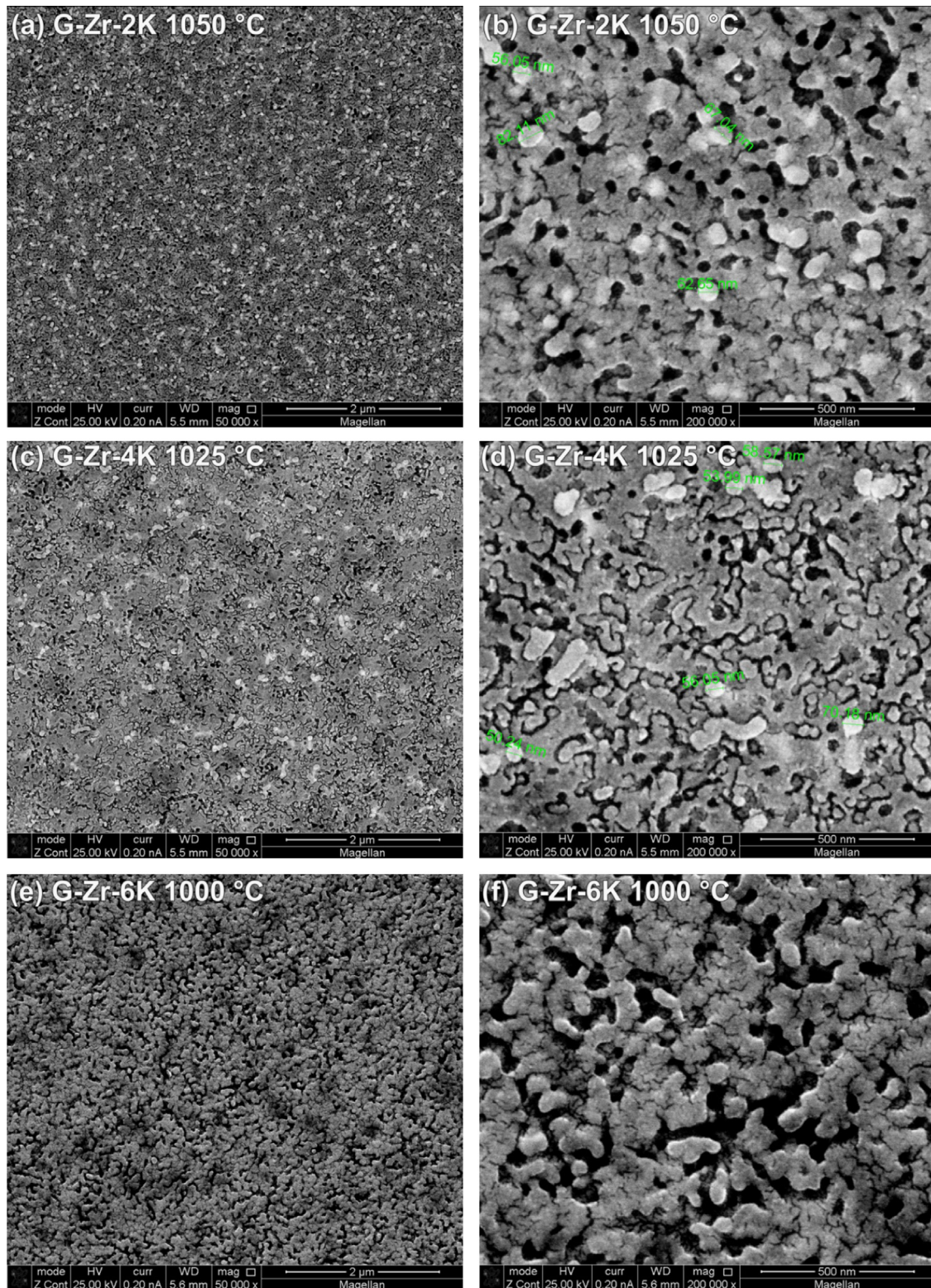


Fig. 10. Back-scattered SEM images of (a and b) G–Zr–2K sintered at 1050 °C, (c and d) G–Zr–4K sintered at 1025 °C and (e and f) G–Zr–6K sintered at 1000 °C (samples etched with 1 wt% HF solution for 40 s).

Hardness and fracture toughness measurements were not possible for samples G and G–Zr due to their high porosity. However, the bending strength increased from 20 to 32 MPa for sample G–Zr compared with the ZrO₂-free base glass.

The microhardness decreased upon increasing the content of K₂O. The bending strength variations exhibited a trend similar to those of the relative density and crystal volume fraction. The sample G–Zr–2K, which exhibited the maximum density, also

Table 4
Mechanical properties, relative density and crystalline volume fraction of sintered specimens.

Glass–ceramics	Temperature (°C)	Relative density (%)	Crystalline volume fraction ^a (%)	Microhardness (Vickers)	3P-bending strength (MPa)	Crack length ^b (μm)	Indentation fracture toughness ^c (MPa m ^{1/2})	Fracture toughness ^d (MPa m ^{1/2})
G	1000	82 ± 1	44 ± 5	–	20 ± 5	–	–	–
G–Zr	1000	78 ± 2	63 ± 7	–	32 ± 6	–	–	–
G–Zr–2K	1050	94 ± 2	55 ± 3	637 ± 41	143 ± 12	24 ± 5	1.3 ± 0.1	1.9 ± 0.1
G–Zr–4K	1025	91 ± 1	32 ± 6	609 ± 44	92 ± 18	28 ± 5	1.1 ± 0.1	1.3 ± 0.2
G–Zr–6K	1000	90 ± 1	12 ± 9	579 ± 63	57 ± 11	40 ± 4	0.8 ± 0.2	0.7 ± 0.2

^aEstimated by Krimm and Tobolsky's method.

^bMeasured from the corner of each indent.

^cEstimated using Niihara's equation.

^dMeasured using single edged notch bending method.

had the highest strength. It was also demonstrated in Fig. 10 that apatite and zirconia are crystallized in this sample and the zirconia content is higher in sample G–Zr–2K than in G–Zr–4K and G–Zr–6K.

A trend analogous to the bending strengths was observed for the fracture toughness. G–Zr–2K showed a maximum toughness of 1.9 MPa m^{1/2}. The value for fracture toughness measured by the SENB method was, in general, higher than the value obtained by the indentation method, which confirms a well-known trend [65].

The average length of the induced crack by indentation for G–Zr–2K was the lowest among all the tested samples (~23 μm), confirming the possible highest value for its toughness. Further K₂O addition decreased the toughness. Furthermore, increasing the K₂O content in this sample retarded the crystallization of zirconia and densification. Therefore, ZrO₂ increases the viscosity and diminishes viscous flow, whereas ZrO₂ crystallization depletes the residual glass in Zr ions and reduces the viscosity. Therefore, it appears that crystallization of ZrO₂ in G–Zr–2K favors the sintering progress and improves the mechanical properties.

Despite the deterioration of the sinterability and inducement of more porosity in sample G–Zr, ZrO₂ increases the average bending strength from 20 to 32 MPa. However, there are many other factors that can increase or decrease the bending strength, such as the pore size, pore shape, or inherent strength of the residual glass.

One or more of the following mechanisms could contribute to the reinforcing effect of zirconia nano-crystals in the glass-ceramic:

(i). Crack deflection by dispersion strengthening. Crack deflection may occur by dispersed zirconia crystals. Fig. 11a–c shows detailed views of polished cross sections of sintered samples after Vickers indentation measurements, in which the crack propagates from the indent corners. In samples G–Zr–2K and G–Zr–4K, the crack length is clearly shorter than that in sample G–Zr–6K (Table 4 and Fig. 11). In sample G–Zr–6K, which contains a high content of residual glass and no ZrO₂ crystals, a straight crack propagated (Fig. 11c). However,

the crack path in samples G–Zr–2K and G–Zr–4K is not straight and shows, to some extent, deflections or bowing near the indentation corner. It should be noted that these samples contain nano-zirconia crystals (Fig. 10a–d), which may be responsible for this crack deflection or blunting of the crack during spreading.

(ii). Transformation toughening by the t-ZrO₂ phase. Several criteria are necessary for effective transformation toughening by tetragonal ZrO₂ in a ceramic matrix: (1) ZrO₂ should not be dissolved by the host; (2) the particle size of ZrO₂ should be smaller than ~0.5 μm; (3) the host microstructure should be stiff enough to retain the ZrO₂ particles in the unstable tetragonal form during cooling; and (4) the amount of retained t-ZrO₂ in the matrix should be higher than 10 mol% (e.g., in a Al₂O₃–ZrO₂ composite) [66,67]. In our study, it is not possible to confirm that the transformation toughening contributes to the improvement of the fracture toughness. However, it can be envisaged that transformation toughening makes little or no contribution to the increased fracture toughness because most of the above mentioned criteria are not satisfied. The nano-zirconia crystals in the matrix of the current glass-ceramics indeed crystallize during heating of the gel-glass. It has been reported that calcium has a great affinity to diffuse from the residual glass into the structure of zirconia, leading to the crystallization of more stabilized t-ZrO₂ [25,26]. We have also detected some amounts of Ca in the ZrO₂ crystals by EDS analysis performed by TEM (Fig. 9). Additionally, the residual glass is not rigid enough to restrain t-ZrO₂ particles. However, overall, the fracture toughness did not improve much.

(iii). Incorporation of Zr⁴⁺ ions into the residual glass structure was confirmed by structural analysis. The presence of Zr ions in the residual glass network, which produce bracing by [ZrO₄]⁴⁻ structural units, may represent another reinforcement mechanism. The NMR results indicate that the average number of Si–O–Si bridges decreases and some new bridges of Si–O–Zr evolve. The substitution of Zr with higher ionic field strength may reinforce the residual glass.

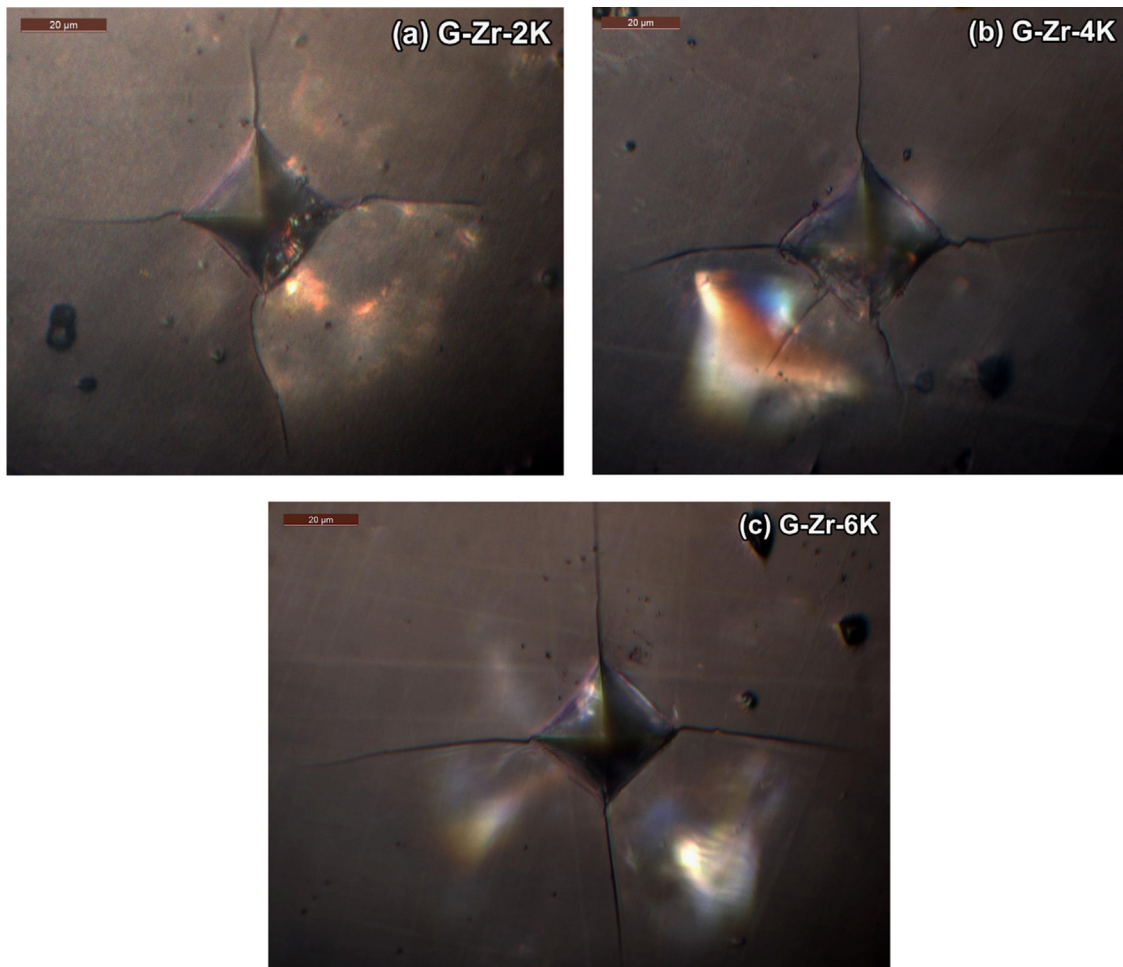


Fig. 11. Crack path induced by Vickers indentation on samples (a) G–Zr–2K, (b) G–Zr–4K and (c) G–Zr–6K.

In general, we suggest that the prevalent mechanism for improved mechanical properties in this study is dispersion strengthening by crack deflection. Homogeneously dispersed nano-zirconia crystals in sample G–Zr–2K leads to increased strength and toughness. However, the bending fracture strengths of G–Zr–4K and G–Zr–6K are lower and represent only slight increases compared with the G–Zr. This result can be attributed to the inadequate densification and crystallization of these samples.

3.6. *In vitro* bioactivity

The SEM images obtained from the surfaces of sintered samples G, G–Zr and G–Zr–2K before and after exposure to SBF at various testing times are presented in Fig. 12a–f. Spherical particles of apatite can be observed on the surface of samples G and G–Zr after 24 h of soaking in SBF. From Fig. 12b and d, it can be concluded that the formation of HCA in these samples is well established. On the G–Zr–2K surface, white and very fine aggregates scattered over the surface are observed after 21 days of soaking in SBF. These fine agglomerated fine particles can be attributed to the formation of apatite nuclei. Furthermore, no noteworthy modifications

were identified on the surface of samples G–Zr–4K and G–Zr–6K after 21 days of soaking in SBF.

The FTIR spectra from the surfaces of all the sintered samples before and after exposure to SBF are presented in Fig. 13a–c. Before the SBF test, the spectra of all the glass-ceramics were characterized by the presence of two bands at approximately 1100 cm^{-1} and 465 cm^{-1} , which are associated with the asymmetric stretching vibration and bending vibration of Si–O–Si bonds, respectively [14,15,37]. After 24 h for sample G (Fig. 13a) and G–Zr (Fig. 13b), the obtained spectra were similar to the synthetic hydroxycarbonate apatite (HCA) spectrum, with changes related to the intensity of the typical HCA bands, located near 1255 cm^{-1} , 1130 cm^{-1} , 1055 cm^{-1} , 605 cm^{-1} and 560 cm^{-1} [8,14,15,23,37]. The observed increase in the intensity and sharpness of these bands after 3 days is associated with the higher density of the formed HCA layer on the sample surfaces (Fig. 13a and b). The formation of apatite was also monitored by SEM, which confirmed the formation of HCA in samples G and G–Zr after 24 h, respectively (Fig. 12). The FTIR spectra for the sample containing 2–6 mol% K_2O after 21 days of soaking in SBF did not exhibit any noteworthy changes (Fig. 13c), confirming that no modifications occurred after soaking in SBF.

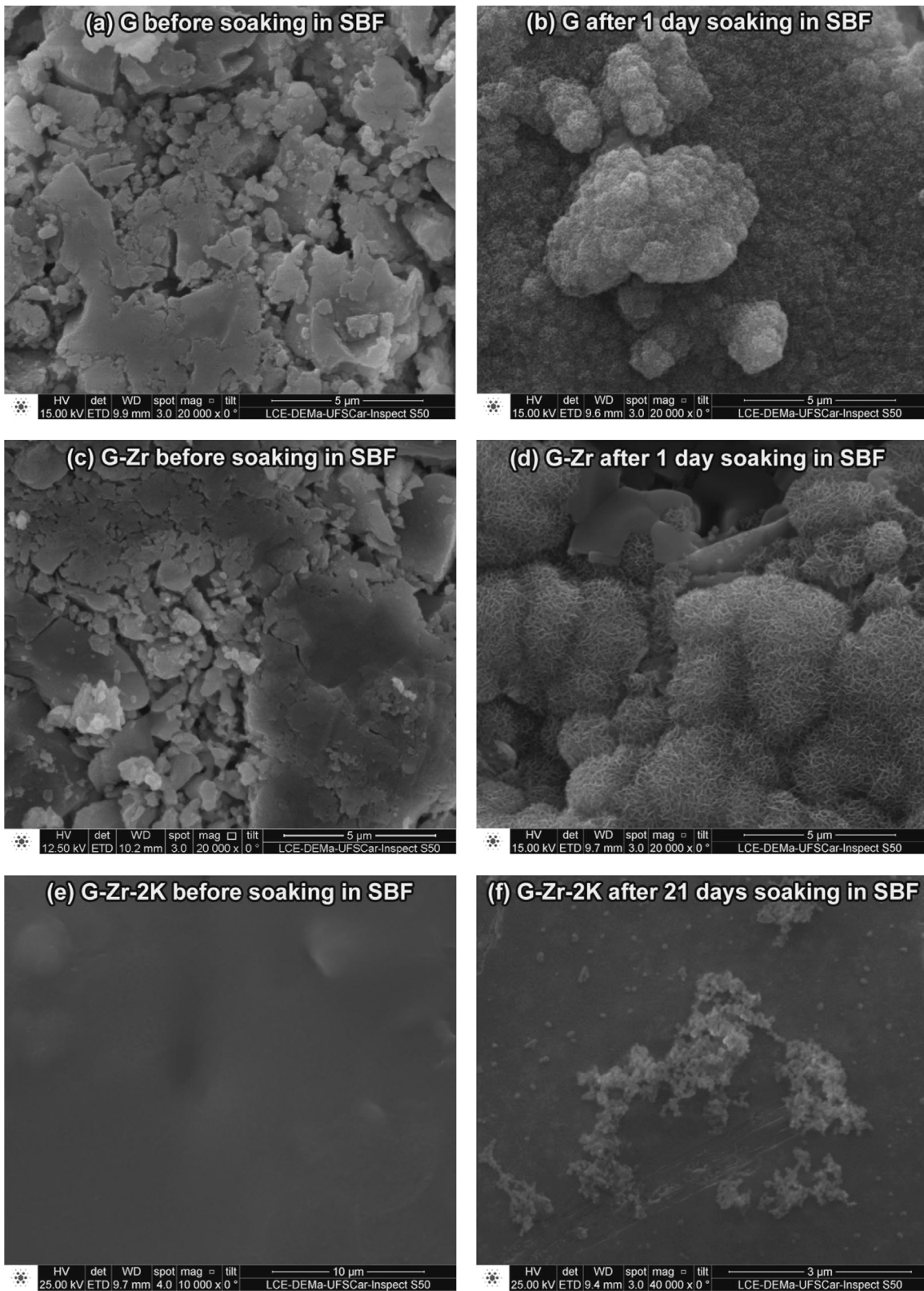


Fig. 12. SEM micrographs from surface of samples (a–b) G, (c–d) G–Zr and (e–f) G–Zr–2K: Before and after 1 day and 21 days exposure to SBF.

The FTIR and SEM analyses confirmed that the sintered glass–ceramics G and G–Zr indeed exhibited *in vitro* bioactivity and lead to apatite formation after 24 h of soaking in

SBF. However, the sintered samples with various K_2O contents do not exhibit any *in vitro* bioactivity. The inertness of these samples containing K_2O can be attributed to their

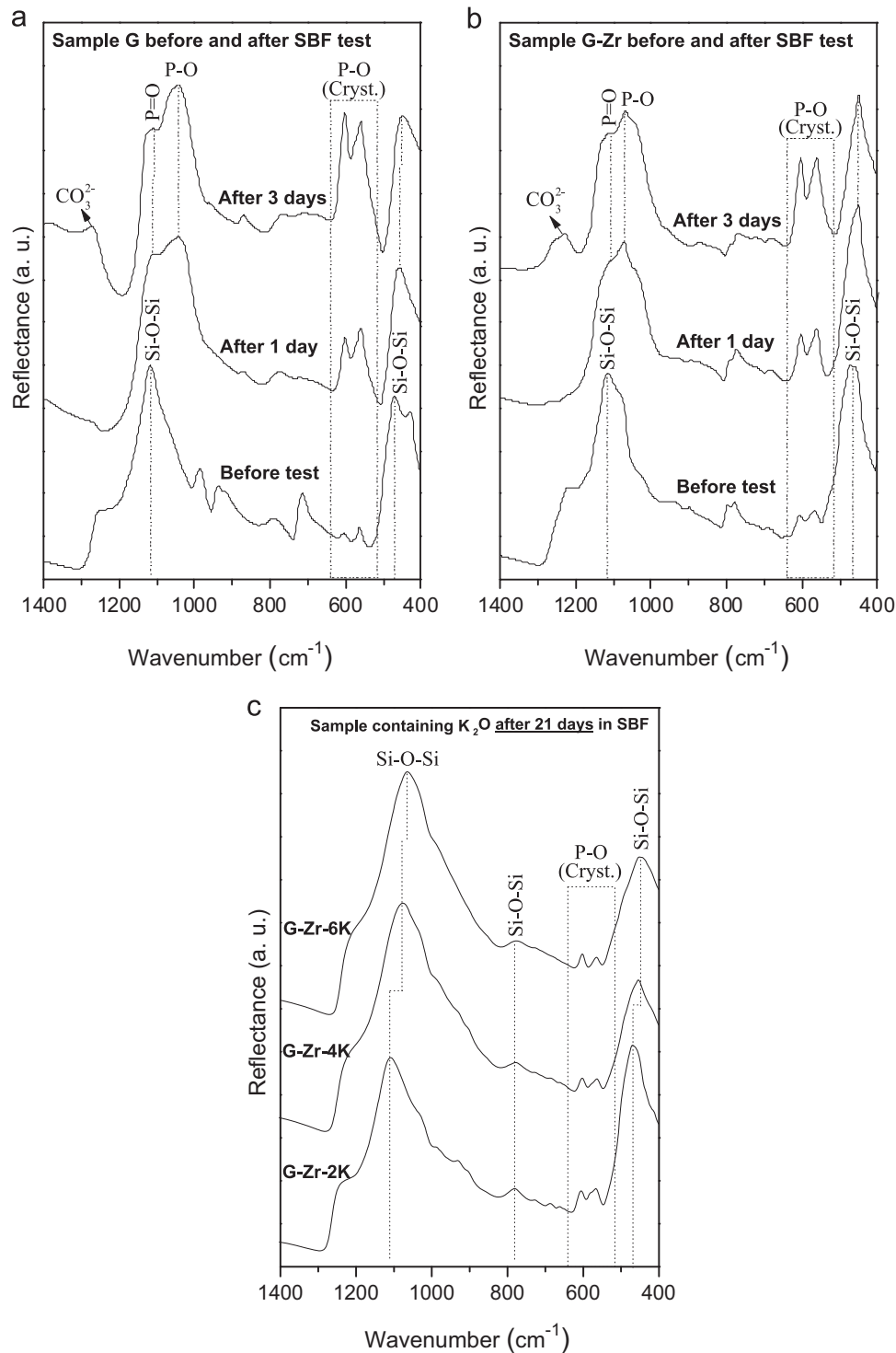


Fig. 13. FTIR spectra of samples G (a), G-Zr (b) and (d) samples containing K_2O before and after soaking in SBF at different testing times.

surface characteristic (open porosity content), residual glass composition and crystalline phases, which affect their solubility and, subsequently, the pH variations of the SBF.

The variations in pH versus soaking time in SBF for all the samples are shown in Fig. 14. For the base glass-ceramic (sample G), the pH range tended to increase throughout the test, whereas for the sample G-Zr, the pH increased only slightly up to 48 h and then remained practically constant. For the samples containing

K_2O , the pH increased slightly after 1 day and then remained almost constant. Keeping in mind that the pH and its variation is a direct consequence of ions released from the sample into the SBF solution, it can be stated that the glass-ceramic G exhibits the highest solubility, and the samples containing K_2O exhibit the lowest solubility, thus maintaining a more stable environment.

It should be noted that samples G and G-Zr contain approximately 18% and 22% porosity, respectively, after heat

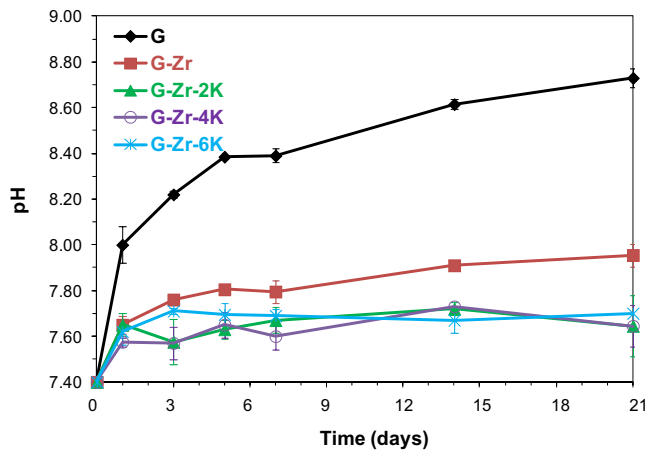


Fig. 14. Variations in pH versus soaking time in SBF.

treatment at 1000 °C. In contrast, samples G-Zr-2K, G-Zr-4K and G-Zr-6K heat-treated at 1050 °C, 1025 °C and 1000 °C respectively, are more dense and present near zero open porosity (closed porosity = 1 - (relative density)), and the open porosity was measured using the water absorption method). Samples G, G-Zr and G-Zr-2K crystallized into an apatite-zirconia glass-ceramic, whereas samples G-Zr-4K and G-Zr-6K were mainly amorphous. It is apparent that the amount of open porosity and degree of crystallization play major roles in activating the bioactivity. The glass-ceramics with high porosity (G and G-Zr) are highly bioactive and contain one highly soluble and bioactive phase, wollastonite [37,64]. Additionally, the crystallization of ZrO₂ in the G-Zr-2K sample encourages the bioactivity. In contrast, the samples containing 4 and 6 mol% K₂O are dense and contain low amounts of zirconia crystals. Therefore, it appears that Zr ions in the residual glass reduce the solubility, diminishing the apatite-forming ability; however, the crystallization of ZrO₂ is helpful for bioactivity. This phenomenon was also observed in our previous study, where the crystallization of zirconia improved the bioactivity compared with the base glass containing dissolved ZrO₂ [37].

4. Proposed applications

In our previous study [37], we developed a bioactive glass and glass-ceramic powders containing 61.2SiO₂-24.3CaO-4.5P₂O₅-10ZrO₂ (mol%) with particular features of bioactivity and radiopacity [37]. In that study, we demonstrated that the ZrO₂-glass and glass-ceramic clearly exhibit increased osteoblast MG-63 cell proliferation [37]. Herein, we demonstrate that partly sintered samples of this same composition are also bioactive and show progressive formation of HCA after a relatively short time (24 h) in SBF (this time is approximately 6 h for the gold standard 45S5 bioglass). In addition, crystallization of zirconia nano-crystals improves the mechanical properties. Therefore, this glass composition can be used for scaffold development or coatings on ZrO₂-based or metal-based dental implants. These new applications have been

suggested recently for gel-derived ZrO₂-containing glasses [32,34,35,68,69].

The K₂O-containing glasses prepared in this study exhibited very good sinterability. The crystalline phases such as zirconia and apatite, which appeared in these glass-ceramics, are appropriate for biocompatibility and mechanical properties. The glass-ceramic containing 2 mol% K₂O was white and opaque, whereas G-Zr-4K and G-Zr-6K were white and translucent. The maximum hardness, strength and toughness measured for sample G-Zr-2K (6% porosity) were 637 ± 41 HV, 143 ± 12 MPa and 1.9 ± 0.1 MPa m^{1/2}, respectively. This material is virtually inert and exhibits very low solubility in SBF. These properties are comparable with those of IPS Cosmo® glass-ceramic, which is used for dentin build-up on a ZrO₂-based core (TZP) in dentistry [2,24]. The main advantage of the current glasses over the existing commercial material is that they can be developed at much lower temperatures, and high-temperature melting can be avoided. The glass compositions are very simple and can be sintered and crystallized simultaneously into apatite-zirconia glass-ceramics at 1000 °C. The zirconia nano-crystals are homogeneously distributed in the matrix, which is good for mechanical performance. However, the disadvantages are that the sol-gel process takes ~10 days, and the residual 6% porosity can lead to staining in the mouth environment.

Therefore, further investigations and improvements are required to determine whether these new glass-ceramics can be used for commercial applications:

- (i). The gelation and aging times need to be decreased from 10 days to a few days. This reduction can be performed by increasing the pH or reducing the water content and must be demonstrated experimentally.
- (ii). The conventional sintering-pressing method, which is used for synthesizing commercial dental glass-ceramics, could be employed to improve the sinterability and may lead to a considerable improvement in the relative density and mechanical properties.
- (iii). The opacity or translucency of the glass-ceramic can be modified by changing the K₂O content or adding new components, such as Na₂O and Li₂O. These new elements can be easily included in the sol-gel process using their nitrate compounds. However, the sintering and crystallization behavior will certainly change, which must be evaluated.
- (iv). Finally, the thermal expansion coefficient should match that of the zirconia core or the implants. This task can be accomplished by changing the amounts of ZrO₂ and K₂O.

All these conditions indicate that these materials are still a long way from market.

5. Conclusions

Apatite-zirconia glass-ceramics were developed via sintering with concurrent crystallization of gel-derived glass powders.

The use of the sol–gel process allowed us to incorporate a high ZrO₂ content in the glass composition, avoiding high-temperature melting.

Glass particle compacts containing 61.2SiO₂–24.3CaO–4.5P₂O₅–10ZrO₂ (mol%) densified to only ~78% of their true density at 1000 °C. The sintered glass–ceramic was bioactive, and apatite formed on its surface after 24 h of soaking in SBF. Crystallization of the zirconia nano-crystals improved the mechanical properties. This type of glass–ceramic is proposed for scaffold development or coatings on ZrO₂-based implants.

The addition of 2–6 mol% K₂O to the base glass extensively improved the sinterability such that densification (RD > 90%) was achieved near 1000 °C. Apatite-like spherical aggregates scattered over the surface of a sample containing 2 mol% K₂O were identified after 21 days in SBF. It appears that crystallization of ZrO₂ in this glass encourages bioactivity compared with the 4–6 mol% K₂O samples, in which the residual glass is a major constituent. These nano-sized tetragonal zirconia crystals were dispersed uniformly within the glass matrix and improved the mechanical properties. We suggest that these materials can be potentially used in dentistry as a restorative build-up on ZrO₂-based cores. Further development is required for this proposed application.

Acknowledgments

The authors are grateful to the São Paulo Research Foundation (FAPESP, 2013/07793-6) Brazil, and the Iran National Science Foundation (INFS, 92007700) for financial support of this research project. We also acknowledge Conselho Nacional de Desenvolvimento Científico e Tecnológico (CNPq), Brazil, and the World Academy of Sciences (TWAS) for funding a Sandwich Ph.D. fellowship for Maziar Montazerian (302976/2013-2). We also greatly thank R. L. Siqueira from CeRTEV for DTA/TG and FTIR measurements.

References

- [1] E.D. Zanotto, A bright future for glass–ceramics, *Am. Ceram. Soc. Bull.* 89 (8) (2010) 19–27.
- [2] V. Marghussian, *Nano-Glass Ceramics: Processing, Properties and Applications*, First Edition, Elsevier, 2015.
- [3] P.W. McMillan, *Glass–Ceramics*, Academic Press, 1979.
- [4] W. Höland, G. Beall, *Glass–Ceramic Technology*, second ed., The American Ceramic Society and A John Wiley & Sons Inc., 2012.
- [5] G.H. Beall, Milestones in glass–ceramics: a personal perspective Special Issue: The Controlled Crystallization of Glass and General Glass Science, *Int. J. Appl. Glas. Sci.* 5 (2) (2014) 93–103.
- [6] J. Zarzycki, Sol–gel Processes in glass making, *Concise Encyclopedia of Semiconducting Materials & Related Technologies*, 1992, pp. 500–504.
- [7] L.L. Hench, Sol–gel materials for bioceramic applications, *Curr. Opin. Solid State Mater. Sci.* 2 (5) (1997) 604–610.
- [8] D. Arcos, M. Vallet-Regí, Review: sol–gel silica-based biomaterials and bone tissue regeneration, *Acta Biomater.* 6 (2010) 2874–2888.
- [9] J.R. Jones, Review of bioactive glass: from hench to hybrids, *Acta Biomater.* 9 (1) (2013) 4457–4486.
- [10] M. Erol-Taygun, K. Zheng, A.R. Boccaccini, Nanoscale bioactive glass in medical application, *Int. J. App. Glass Sci.* 4 (2) (2013) 136–148.
- [11] I. Izquier-Barba, A.J. Salinas, M. Vallet-Regí, Bioactive glasses: from macro to nano, *Int. J. App. Glas. Sci.* 4 (2) (2013) 149–161.
- [12] M. Vallet-Regí, A.J. Salinas, D. Arcos, From the bioactive glasses to the star gels, *J. Mater. Sci.: Mater. Med.* 17 (2006) 1011–1017.
- [13] M. Vallet-Regí, Revisiting ceramics for medical applications, *J. Chem. Soc.* 44 (2006) 5211–5220.
- [14] J. Roman, S. Padilla, M. Vallet-Regí, Sol–gel glasses as precursors of bioactive glass-ceramics, *Chem. Mater.* 15 (2003) 798–806.
- [15] R.L. Siqueira, E.D. Zanotto, The influence of phosphorus precursors on the synthesis and bioactivity of SiO₂–CaO–P₂O₅ sol–gel glasses and glass-ceramics, *J. Mater. Sci.: Mater. Med.* 24 (2013) 365–379.
- [16] E.D. Zanotto, The formation of unusual glasses by sol–gel processing, *J. Non-Cryst. Solids* 147–148 (1992) 820–823.
- [17] M. Montazerian, Effect of ZrO₂ addition on properties of gel-derived bioactive SiO₂–CaO–P₂O₅ glass–ceramics (Ph.D. dissertation), Iran University of Science and Technology, 2015.
- [18] H.C. Li, D.G. Wang, J.H. Hu, C.Z. Chen, Crystallization, mechanical properties and in vitro bioactivity of sol–gel derived Na₂O–CaO–SiO₂–P₂O₅ glass–ceramics by partial substitution of CaF₂ for CaO, *Sol–Gel Sci. Technol.* 67 (2013) 56–65.
- [19] M. Łączka, K. Cholewa-Kowalska, A. Łączka-Osyczka, M. Tworzydło, B. Turyna, Gel-derived materials of a CaO–P₂O₅–SiO₂ system modified by boron, sodium, magnesium, aluminum, and fluorine compounds, *J. Biomed. Mater. Res.* 52 (2000) 601–612.
- [20] X. Yang, L. Zhang, X. Chen, X. Sun, G. Yang, X. Guo, H. Yang, C. Gao, Z. Gou, Incorporation of B₂O₃ in CaO–SiO₂–P₂O₅ bioactive glass system for improving strength of low-temperature co-fired porous glass ceramics, *J. Non-Cryst. Solids* 358 (2012) 1171–1179.
- [21] H.C. Li, D.G. Wang, J.H. Hu, C.Z. Chen, Effect of the partial substitution of K₂O, MgO, B₂O₃ for CaO on crystallization, structure and properties of Na₂O–CaO–SiO₂–P₂O₅ system glass–ceramic, *Mater. Lett.* 106 (2013) 373–376.
- [22] X. Chatzistavrou, D. Esteve, E. Hatzistavrou, E. Kontonasaki K.M. Parakevopoulos, A.R. Boccaccini, Sol–gel based fabrication of novel glass-ceramics and composites for dental applications, *J. Mater. Sci. Eng. C* 30 (2010) 730–739.
- [23] D. Bellucci, A. Sola, R. Salvatori, A. Anesi, L. Chiarini, V. Cannillo, Sol–gel derived bioactive glasses with low tendency to crystallize: synthesis, post-sintering bioactivity and possible application for the production of porous scaffolds, *Mater. Sci. Eng. C* 43 (2014) 573–586.
- [24] M. Schweiger, M. Frank, C.V. Clausbruch, W. Höland, V. Rheinberger, Microstructure and properties of a composite system for dental applications composed of glass–ceramics in the SiO₂–LiO₂–ZrO₂–P₂O₅ system and ZrO₂-ceramic (TZP), *J. Mater. Sci.* 34 (1999) 4563–4572.
- [25] T. Kasuga, M. Yoshida, A.J. Ikushima, M. Tuchiya, H. Kusakari, Bioactivity of zirconia-toughened glass-ceramics, *J. Am. Ceram. Soc.* 75 (7) (1992) 1884–1888.
- [26] T. Kasuga, K. Nakajima, T. Uno, M. Yoshida, Preparation of zirconia-toughened bioactive glass–ceramic composite sinter-hot isostatic pressing, *J. Am. Ceram. Soc.* 75 (1992) 1103–1107.
- [27] D. Mondal, S. So-Ra, B.T. Lee, Fabrication and characterization of ZrO₂–CaO–P₂O₅–Na₂O–SiO₂ bioactive glass ceramics, *J. Mater. Sci.* 48 (5) (2013) 1863–1872.
- [28] M. Montazerian, P. Alizadeh, B. Eftekhari Yekta, Pressureless sintering and mechanical properties of mica glass–ceramic/Y-PSZ composite, *J. Eur. Ceram. Soc.* 28 (2008) 2687–2692.
- [29] M. Montazerian, P. Alizadeh, B. Eftekhari Yekta, Processing and properties of a mica–apatite glass–ceramic reinforced with Y-PSZ particles, *J. Eur. Ceram. Soc.* 28 (2008) 2693–2699.
- [30] E. Verné, R. Defilippi, G. Carl, C. Vitale Brovarone, P. Appendino, Viscous flow sintering of bioactive glass–ceramic composites toughened by zirconia particles, *J. Eur. Ceram. Soc.* 23 (2003) 675–683.
- [31] M. Ghaffari, P. Alizadeh, M.R. Rahimpour, Sintering behavior and mechanical properties of mica–diopside glass–ceramic composites reinforced by nano and micro-sized zirconia particles, *J. Non-Cryst. Solids* 358 (23) (2012) 3304–3311.
- [32] Y. Zhu, Y. Zhang, C. Wu, Y. Fang, J. Yang, S. Wang, The effect of zirconium incorporation on the physicochemical and biological properties

- of mesoporous bioactive glasses scaffolds, *Microporous Mesoporous Mater.* 143 (2011) 311–319.
- [33] C. Persson, E. Unosson, I. Ajaxon, J. Engstrand, H. Engqvist, W. Xia, Nano grain sized zirconia–silica glass–ceramics for dental applications, *J. Eur. Ceram. Soc.* 32 (16) (2012) 4105–4110.
- [34] K.P. Ananth, S. Suganya, D. Mangalaraj, J.M.F. Ferreira, A. Balamurugan, Electrophoretic bilayer deposition of zirconia and reinforced bioglass system on Ti6Al4V for implant applications: an *in vitro* investigation, *J. Mater. Sci. Eng. C* 33 (2013) 4160–4166.
- [35] F. Tallia, M. Gallo, L. Pontiroli, F. Baino, S. Fiorilli, B. Onida G.C. Anselmetti, A. Manca, C. Vitale-Brovarone, Zirconia-containing radiopaque mesoporous bioactive glasses, *Mater. Lett.* 130 (2014) 281–284.
- [36] C. Vitale-Brovarone, E. Verné, M. Bergui, B. Onida, F. Baino, M. Miola, et al. Injectable osteoinductive bone cements, World Patent Application, WO 2011141889 A1.
- [37] M. Montazerian, B. EftekhariYekta, V.K. Marghussian, C.F. Bellani, R. L. Siqueira, E.D. Zanotto, Bioactivity and cell proliferation in radiopaque gel-derived CaO-P₂O₅-SiO₂-ZrO₂ glass and glass-ceramic powders, *J. Mater. Sci. Eng. C* (2015), <http://dx.doi.org/10.1016/j.msec.2015.05.065>.
- [38] S. Krimm, A.V. Tobolsky, Quantitative X-ray studies of order in amorphous and crystalline polymers. Quantitative X-ray determination of crystallinity in polyethylene, *J. Polym. Sci.* 7 (1951) 57–76.
- [39] Standard Test Method for Water Absorption, Bulk Density, Apparent Porosity, and Apparent Specific Gravity of Fired Whiteware Products, Ceramic Tiles, and Glass Tiles. ASTM C373-14a.
- [40] K. Niihara, R. Morena, D.P.H. Hasselman, in: R.C. Bradt, A.G. Evans, P.P. Hassehnan, F.F. Lange (Eds.), *Fracture Mechanics of Ceramics*, vol. 5, Plenum, New York, 1983, pp. 97–105.
- [41] K. Niihara, A. Nakahira, T. Hirai, The effect of stoichiometry on mechanical properties of boron carbide, *J. Am. Ceram. Soc.* 67 (1) (1984) C-13–C-14.
- [42] Standard Test Method for Linear-Elastic Plane-Strain Fracture Toughness K_{IC} of Metallic Materials. ASTM E399—12e3.
- [43] H. Wang, G. Isgro, P. Pallav, A.J. Feilzer, Influence of test methods on fracture toughness of a dental porcelain and a soda lime glass, *J. Am. Ceram. Soc.* 88 (10) (2005) 2868–2873.
- [44] T. Kokubo, H. Takadama, How useful is SBF in predicting *in vivo* bone bioactivity?, *Biomaterials* 27 (2006) 2907–2915.
- [45] A.L.B. Maçon, T.B. Kim, E.M. Valliant, K. Goetschius, R.K. Brow D.E. Day, A. Hoppe, A.R. Boccaccini, I.Y. Kim, C. Ohtsuki, T. Kokubo, A. Osaka, M. Vallet-Regí, D. Arcos, L. Fraile, A.J. Salinas, A. V. Teixeira, Y. Vueva, R.M. Almeida, M. Miola, C. Vitale-Brovarone, E. Verné, W. Höland, J.R. Jones, A unified *in vitro* evaluation for apatite-forming ability of bioactive glasses and their variants, *J. Mater. Sci.: Mater. Med.* 26 (2015) 115–125.
- [46] H. Aguiar, J. Serra, P. Gonzalez, B. Leon, Influence of the stabilization temperature on the structure of bioactive sol–gel silicate glasses, *J. Am. Ceram. Soc.* 93 (8) (2010) 2286–2291.
- [47] S. Lin, C. Ionescu, K.J. Pike, M.E. Smith, J.R. Jones, Nanostructure evolution and calcium distribution in sol–gel derived bioactive glass, *J. Mater. Chem.* 19 (2009) 1276–1282.
- [48] D. Arcos, D.C. Greenspan, M. Vallet-Regí, Influence of the stabilization temperature on textural and structural features and ion release in SiO₂-CaO-P₂O₅ sol–gel glasses, *Chem. Mater.* 14 (2002) 1515–1522.
- [49] A.J. Salinas, A.I. Martín, M. Vallet-Regí, Bioactivity of three CaO-P₂O₅-SiO₂ sol–gel glasses, *J. Biomed. Mater. Res.* 61 (2002) 524–532.
- [50] S. Padilla, J. Román, A. Carenas, M. Vallet-Regí, Influence of the phosphorus content on the bioactivity in sol–gel glass ceramics, *Biomaterials* 26 (2005) 475–483.
- [51] A. Martínez, I. Izquierdo-Barba, M. Vallet-Regí, Bioactivity of a CaO-SiO₂ binary glasses system, *Chem. Mater.* 12 (2000) 3080–3088.
- [52] I. Izquierdo-Barba, A.J. Salinas, M. Vallet-Regí, *In vitro* calcium phosphate layer formation on sol–gel glasses of the system CaO-SiO₂, *J. Biomed. Mater. Res.* 47 (1999) 243–250.
- [53] A. García, M. Cicuéndez, I. Izquierdo-Barba, D.M. Arcos, M. Vallet-Regí, Essential role of calcium phosphate heterogeneities in 2D-hexagonal and 3D cubic SiO₂-CaO-P₂O₅ mesoporous bioactive Glasses, *Chem. Mater.* 21 (22) (2009) 5474–5484.
- [54] M. Vallet-Regí, A.J. Salinas, J. Ramírez-Castellanos, J.M. González-Calbet, Nanostructure of bioactive sol–gel glasses and organic–inorganic hybrids, *Chem. Mater.* 17 (2005) 1874–1879.
- [55] E. Leonova, I. Izquierdo-Barba, D. Arcos, A. López-Noriega, N. Hedi, M. Vallet-Regí, Multinuclear solid-state NMR studies of ordered mesoporous bioactive glasses, *J. Phys. Chem. C* 112 (2008) 5552–5562.
- [56] J. Serra, P. González, S. Liste, C. Serra, S. Chiussi, B. León, M. Pérez-Amor, H.O. Ylänen, M. Hupa, FTIR and XPS studies of bioactive silica based glasses, *J. Non-Cryst. Solids* 332 (2003) 20–27.
- [57] H. Maekawa, T. Maekawa, K. Kawamura, T. Yokokawa, The structural groups of alkali silicate glasses determined from ²⁹Si MAS-NMR, *J. Non-Cryst. Solids* 127 (1) (1991) 53–64.
- [58] L. Barbieri, V. Cannillo, C. Leonelli, M. Montorsi, P. Mustarelli, C. Siligardi, Experimental and MD simulations study of CaO-ZrO₂-SiO₂ glasses, *J. Phys. Chem. B* 107 (2003) 6519–6525.
- [59] M. Nogami, Glass preparation of the ZrO₂-SiO₂ system by the sol–gel process from metal alkoxides, *J. Non-Cryst. Solids* 69 (1985) 415–423.
- [60] K. Okasaka, H. Nasu, K. Kamiya, Investigation of coordination state of Zr⁴⁺ ions in the sol-gel-derived ZrO₂-SiO₂ glasses by EXAFS, *J. Non-Cryst. Solids* 136 (1991) 103–110.
- [61] M.W.G. Lockyer, D. Holland, R. Dupree, NMR investigation of the structure of some bioactive and related glasses, *J. Non-Cryst. Solids* 188 (3) (1995) 207–219.
- [62] M. Manda, O. Goudouri, L. Papadopoulou, N. Kantiranis, D. Christofilos, K. Triantafyllidis, K. Chrissafis, K.M. Paraskevopoulos, P. Koidis, The effect of high tempered firing cycle on the bioactive behavior of sol–gel derived dental porcelain modified by bioactive glass, *J. Sol–Gel Sci. Technol.* 63 (2012) 481–494.
- [63] J. Ma, C.Z. Chen, D.G. Wang, X.G. Meng, J.Z. Shi, Influence of the sintering temperature on the structural feature and bioactivity of sol-gel derived SiO₂-CaO-P₂O₅ bioglass, *Ceram. Int.* 36 (6) (2010) 1911–1916.
- [64] S.Y. Ni, J. Chang, L. Chou, A novel bioactive porous CaSiO₃ scaffold for bone tissue engineering, *J. Biomed. Mater. Res. Part A* 76 (2006) 196–205.
- [65] F.C. Serbena, I. Mathias, C.E. Foerster, E.D. Zanotto, Crystallization toughening of a model glass-ceramic, *Acta Mater.* 86 (2015) 216–228.
- [66] R.H.J. Hannink, P.M. Kelly, B.C. Muddle, Transformation toughening in zirconia-containing ceramics, *J. Am. Ceram. Soc.* 83 (2000) 461–487.
- [67] D.W. Richerson, *Modern Ceramic Engineering*, Marcel Dekker, New York, 1992, p. 731–762.
- [68] S.M. Rabiee, M. Azizian, Effect of zirconia concentration on the growth of nanowires in bioactive glass–ceramic coatings, *Int. J. Appl. Ceram. Tech.* 10 (1) (2013) 33–39.
- [69] M. Prabhu, K. Kavitha, S. Sutha, P. Manivasakan, V. Rajendran, P. Kulandaivelu, K. Alameh, Bioactivity of zirconium-substituted nano-bioactive glass particles, *Synth. Reactivity Inorg., Metal-Organic Nano-Metal Chem.* 45 (1) (2015) 92–96.